Exploiting Elastic Energy Storage for "Blind" Cyclic Manipulation: Modeling, Stability Analysis, Control, and Experiments for Dribbling

Sami Haddadin ⓘ, *Member, IEEE*, Kai Krieger ⓘ, Alin Albu-Schäffer ⓘ, *Fellow, IEEE*, and Torsten Lilge ⓘ

Abstract—For creating robots that are capable of human-like performance in terms of speed, energetic properties, and robustness, intrinsic compliance is a promising design element. In this paper, we investigate the principle effects of elastic energy storage and release for basketball dribbling in terms of open-loop cycle stability. We base the analysis, which is performed for the 1-degree-of-freedom (DoF) case, on error propagation, peak power performance during hand contact, and robustness with respect to varying hand stiffness. As the ball can only be controlled during contact, an intrinsically elastic hand extends the contact time and improves the energetic characteristics of the process. To back up our basic insights, we extend the 1-DoF controller to 6-DoFs and show how passive compliance can be exploited for a 6-DoF cyclic ball dribbling task with a 7-DoF articulated Cartesian impedance controlled robot. As a human is able to dribble blindly, we decided to focus on the case of contact force sensing only, i.e., no visual information is necessary in our approach. We show via simulation and experiment that it is possible to achieve a stable dynamic cycle based on the 1-DoF analysis for the primary vertical axis together with control strategies for the secondary translations and rotations of the task. The scheme allows also the continuous tracking of a desired dribbling height and horizontal position. The approach is also used to hypothesize about human dribbling and is validated with captured data.

Index Terms—Cycle stability analysis, disturbance observer, elastic energy storage, flexible joint manipulators, limit cycles, variable stiffness actuation.

I. INTRODUCTION

ACTIVELY compliant robots have found their way to market with the launch of the DLR lightweight robot III (LWR-III) [1] that was commercialized as the KUKA lightweight robot. More recent examples are the Sawyer robot from Rethink Robotics [2], and Panda from FRANKA EMIKA [3]. These robots make it possible to dexterously manipulate objects and to interact with dynamic and (partially) unknown environments. Along this line of research the design of systems with intrinsic, i.e., passive compliance has drawn significant attention. The approach has been motivated by the possibility to provide compliant behavior for the entire mechanical bandwidth. This is of course much larger than the one of an active compliance loop, which is limited by the sensor, actuator, and controller bandwidths. Furthermore, good shock resistance and the ability to dynamically store and release energy are main motivations for the design choice. The latter was recently exploited for explosive motions as, e.g., in throwing [4]. Based on an optimal control formulation the use of joint elasticity enables the robot to reach link speeds that are significantly larger than the maximum motor speed. In this paper, we exploit intrinsic elasticity for cyclic object manipulation based on ball dribbling with an intrinsically and actively compliant robot, see Fig. 1.

Related object manipulation problems, which are in general hybrid,[1] have been investigated for quite some time. Robot dribbling, e.g., was first introduced in [5]. The authors used a horizontal, half-cylindrical tube as end-effector for mapping the system to a rigid two-dimensional (2-D) problem. The control is reactive and pushes the ball downwards if a contact is detected while, depending on the contact position, a spin is also applied.[2] In [6], a high-speed multifingered hand for dribbling a ping-pong ball with high-speed vision is utilized. This experiment was used to evaluate high-speed vision for ball tracking. The work [7] introduced a dribbling industrial robot, utilizing a solid plate as hand. The control mainly relies on the ball tracking vision system and achieves stability of the cycle. A comparison between visual and force/torque feedback is provided in [8], where the vision-based control led to better results. However, as shown in the present work, this is mainly caused by missing

---

[1] We refer to discrete switching between contact and noncontact situations, where hybrid systems theory can be applied.

[2] As the referenced publication is only a video, it is not exactly clear which degrees of freedom (DoF) are purposely controlled.
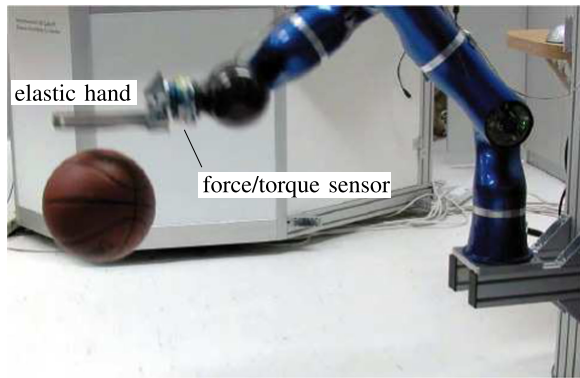
Fig. 1.   Dribbling blindly with a robot arm equipped with an elastic hand.

elasticities leading to very short contact intervals with according force/torque measurements and consequently only little information. In [9], some theoretical analysis was given for using an elastic contact element based on an optimal control trajectory. However, only the vertical movement and a fixed stiffness of the elastic element is considered. This also holds for [10], where the resonance of a long elastic beam is used in its second mode for dribbling or juggling.

The classical juggling task, which is closely related to dribbling, was first treated in [11]. The found solution is a mirrored and scaled version of the ball trajectory, which means that the ball has to be tracked over the entire cycle. In [12] the first blindly juggling robot was presented. The approach presented in [13] used only a linear motor for juggling without the need of active ball tracking or other feedback, as the lateral motion is stabilized by the shape of the juggling paddle. The authors compared an $\mathcal{H}_2$ optimal controller with the previous open-loop solution, which turned out to have similar performance characteristics.

In this paper, which extends prior work in [14] and [15], we provide insights into the problem of *blind*, i.e., without visual information, and *elastic* dribbling. This is an interesting problem in order to further understand how intrinsic elasticity can be used to achieve high performance and energy efficiency during dynamic and/or repetitive tasks such as throwing [4], walking [16], and batting [17]. In this context, several questions arise when intrinsic elasticity is taken into account. A particularly important one is how to select the spring stiffness for optimally achieving a given task. Our aim is to analyze this for the dribbling problem, as this poses high demands on the robot in terms of speed, dexterity, and robustness. A rather intuitive benefit why compliance is desired for this task, which however has not been shown up to now, is that the robot should be able to sustain longer ball contact over an extended time period compared to stiff robots. In turn, this would yield a better opportunity to robustly control the ball, which was already utilized in [9]. However, a further consideration that is still to be validated is that the energy transfer between robot and ball should be a much slower process and, thus, require less peak power when the hand stiffness gets smaller. Before treating these essential questions, we first provide a framework for evaluating the open-loop stability of the resulting dribbling cycles in the 1-DoF case. Subsequently, we

develop an observer based method for tracking and predicting the ball trajectory based on proprioceptive force sensing only and provide a stability analysis.

At full scale, we consider the problem of a rather stiff Cartesian impedance controlled lightweight arm that is equipped with an intrinsically compliant hand in order to provide the desired elasticity at full bandwidth. Based on the basic 1-DoF analysis, we extend the controller to a full 6-DoF elastic dribbling controller, i.e., all degrees of freedom of the robot's end-effector are utilized for control. The extension to the full dimensional problem enables also the stable tracking of dribbling at a desired position and height.[3] Finally, we perform simulations and experiments for the validation of the presented methods, including the systematic analysis and explanation of human dribbling by applying the framework derived in this paper.

Compared to [14] and [15], we provide additional significant contributions. For the disturbance observer, that is used for estimating the end-effector acceleration, a convergence analysis and a stability proof are given and new insights into the used compensation of dynamic load and external torques are provided. Moreover, we present a validation of our approach with experimental data captured from human dribbling. The parameters of the presumed hand trajectory were found such that the mean squared error between resulting ball motion and the measured data is minimized and the stability margin of the resulting cycle is analyzed. For this, we extend the excitation trajectory of the hand by a variable relation p of positive and negative sine half-wave. The achieved explanation of human dribbling constitutes a promising result and might lead to a general framework for analyzing and optimizing human dribbling motions.

This paper is organized as follows. Section II introduces the considered 1-DoF hybrid system and its extension to the full 6-DoF case. Section III provides the solution trajectory for a periodic cycle and analyzes the cycle stability together with energetic considerations. Then, in Section IV, we give a solution for estimating the ball state by a hybrid observer. Furthermore, the extension of the 1-DoF observer to all three translations with an associated reference control scheme for the lateral ball motion is introduced, where an acceleration observer allows the estimation of contact forces. For validation of our methods, they are used to analyze and explain the stability of human dribbling in Section V. In addition, dribbling simulations and dribbling experiments with a 7-DoF DLR lightweight robot III (LWR-III) are presented. Finally, this paper concludes with Section VI. The experimental evaluation of our work can be found in the accompanying video attachment.

II. MODELING

This section provides the analytical models of the ball and the robot required for describing and analyzing the dribbling motion. We outline a suitable 1-DoF model for analyzing the essentials of the periodic dribbling task. Furthermore, we show its extension to a full 6-DoF model, which includes the ball and hand model as well as the floor and hand contact of the ball.

---

[3]In fact, our scheme allows also to adjust the dribbling frequency and amplitude. However, this is omitted for brevity in this paper.
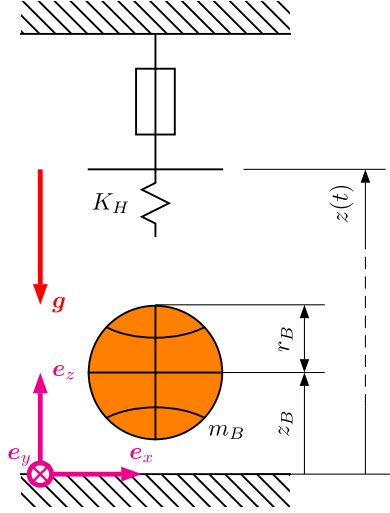
Fig. 2.   Model of the considered 1-DoF dribbling task.

Fig. 3.   Directed graph of the hybrid dribbling model.

A. 1-DoF Dribbling Model

Fig. 2 depicts a schematic illustration of the considered system. The ball is modeled as a point mass m_B with radius r_B and gravity g that can perform vertical movements denoted by the ball height z_B. The hand position is $z(t)$. In this paper, we consider the hand to be elastic and having zero mass. The associated stiffness K_H is attached to the hand. Since the ball stiffness is much larger than the hand stiffness, we may assume the ball to be a rigid object during hand contact. Please note that we consider physical springs and not actively controlled elastic behavior, as no available robot is able to provide the necessary control bandwidth for such high-speed motions. As the spring is considered to be much more compliant than the robot, we may assume the robot to be a position actuator. We use this simplified robot model as we want to study the essential elements of the vertical elastic dribbling cycles.

The ball motion is modeled as a hybrid system. One state node represents the ball being in free flight. Defining the state vector $\boldsymbol{z}_B := [z_{1B} \, z_{2B}]^T = [z_B \, \dot{z}_B]^T$, we obtain the state-space equation of motion for free flight as

$$\dot{\boldsymbol{z}}_B = \boldsymbol{f}_1(\boldsymbol{z}_B) = \begin{bmatrix} z_{2B} \\ -g \end{bmatrix}. \qquad (1)$$

The equation of motion within the state node during hand contact is characterized by the linear spring with an anchor point moving with the desired position $z(t)$. Hence, during hand contact $\boldsymbol{z}_B$ is described by

$$\dot{\boldsymbol{z}}_B = \boldsymbol{f}_2(\boldsymbol{z}_B, t) = \begin{bmatrix} z_{2B} \\ -\frac{K_H}{m_B}(z_{1B} + r_B - z(t)) - g \end{bmatrix}. \qquad (2)$$

Based on the instantaneous ball position, the hybrid system switches between these two state nodes. Finally, if the condition $z_{1B} + r_B \geq z(t)$ is fulfilled the ball is in contact with the hand.

The floor is modeled by an instantaneous transition into the same state (free flight) in the hybrid system, as the position before and after ground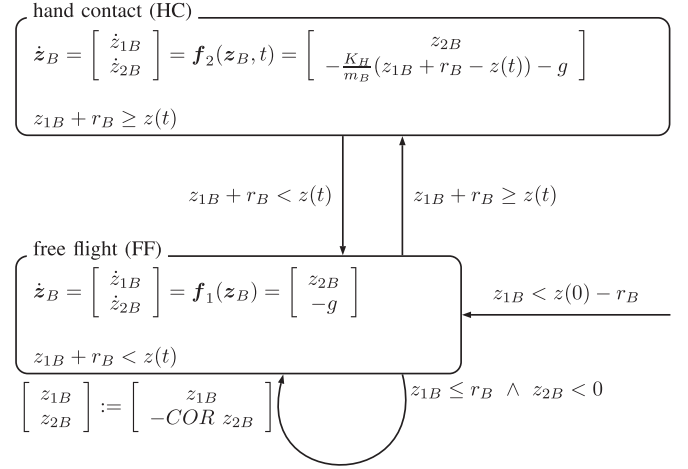 contact remains practically the same, whereas the velocity changes its sign and looses magnitude. The ground contact is typically in the range of 0.015 s (for a drop height of 1 m), i.e., negligible compared to the overall dribbling cycle [18]. Hence, we introduce a coefficient of restitution (COR) that is defined as

$$\text{COR} := -\frac{z_{2B}^+}{z_{2B}^-} \qquad (3)$$

with z_{2B}^- being the velocity before and z_{2B}^+ the velocity after contact, see [19]. This instant takes place if the ball reaches the height $z_{1B} = r_B$ with $z_{2B} < 0$. The parameter COR is chosen to be 0.85 according to the official rules of basketball [20], where the inflation of the ball is defined based on the rebounded height.

Overall, the described model can be represented by the directed graph depicted in Fig. 3. For convenience, the ball is initialized in free-flight state.

Next, we outline the ball and hand model suitable for the 6-DoF dribbling task.

B. 6-DoF Dribbling Model

A schematic view of the 6-DoF model is depicted in Fig. 4. In reality, we use three fingers that are mounted along one common plane, cf., Fig. 5. The fingers are made of spring steel, while for impact damping issues a thin foam layer is glued to them. Please note, that the outer fingers are slightly tilted in order to improve the lateral stability of the ball motion between the dribbling cycles.

In the modeling part, we assume the fingers to be massless and use only their respective spring characteristics, cf., Fig. 4. Both bodies are described by their respective position and orientation. The relevant frames are the end-effector frame $\{EE\}$, the world frame $\{W\}$ (located on the floor), and the robot's base frame $\{0\}$ (above the world frame). The spring mounting is translated into the $\{EE\}$ frame by the offsets δ_z and δ_x.

In the following, we derive a suitable ball model and show how to obtain the relevant forces acting on the ball. All vectors
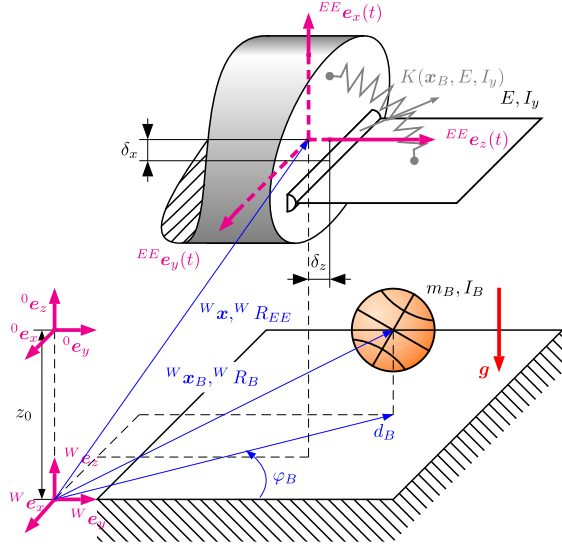
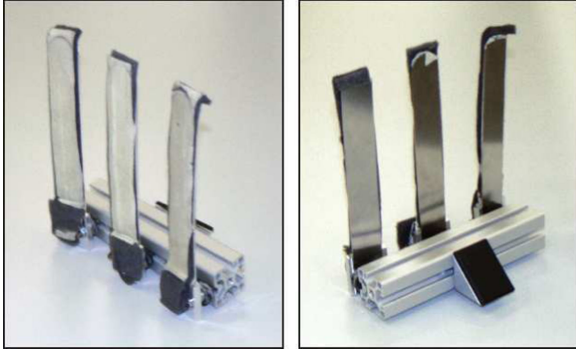Fig. 4. Definitions and conventions for the overall 6-DoF hand-ball model.

Fig. 5. Elastic dribbling hand used for the experiments with the DLR Lightweight-Robot III.

are expressed in $\{W\}$ unless specified otherwise. Hence, we drop the index for this frame subsequently.

The ball is modeled as a free body with gravity vector $\boldsymbol{g}$ and contact force $\boldsymbol{F}_B$ acting on its perimeter. It is described by three translational coordinates $\boldsymbol{x}_B = [x_B \; y_B \; z_B]^T$, the respective velocity $\dot{\boldsymbol{x}}_B$, the quaternion $\boldsymbol{\xi}_B = [q_0 \; q_1 \; q_2 \; q_3]^T$, and three rotational velocities $\boldsymbol{\omega}_B = [\alpha_B \; \beta_B \; \gamma_B]^T$ about the axes of $\{W\}$. Its equation of motion is

$$
\begin{bmatrix}
\ddot{\boldsymbol{x}}_B \\
\dot{\boldsymbol{\xi}}_B \\
\dot{\boldsymbol{\omega}}_B
\end{bmatrix}
=
\begin{bmatrix}
\dfrac{1}{m_B}\boldsymbol{F}_B + \boldsymbol{g} \\
\dfrac{1}{2}Q(\boldsymbol{\xi}_B)\boldsymbol{\omega}_B \\
I_B^{-1}(\boldsymbol{r}_B \times \boldsymbol{F}_B)
\end{bmatrix}
\tag{4}
$$

with $\boldsymbol{r}_B$ being the vector[4] from the ball center to the force application point, m_B the ball mass, and I_B the ball inertia tensor, which is diagonal due to the ball's rotational symmetry. $Q(\boldsymbol{\xi}_B)$ is a matrix that maps Cartesian velocities $\boldsymbol{\omega}_B$ to quaternion

[4]Position vectors are in general denoted by $\boldsymbol{r}$ throughout this paper.

velocities [21]. The ball's attitude described by the quaternion $\boldsymbol{\xi}_B$ is included in our simulation, e.g., for the tangential force during hand- or floor contact described by the LuGre model (8). However, the control design is not based on the attitude. The calculation of the force $\boldsymbol{F}_B$ for the different phases is shown in the following paragraphs.

For the control presented later it is useful to have the translational coordinates also in cylindrical form $\boldsymbol{x}_{B_C} = [\varphi_B \; d_B \; z_B]^T$, see Fig. 4. These are obtained via

$$
\boldsymbol{x}_{B_C} =
\begin{bmatrix}
\varphi_B \\
d_B \\
z_B
\end{bmatrix}
=
\begin{bmatrix}
\arctan_2(-x_B, y_B) \\
\sqrt{x_B^2 + y_B^2} \\
z_B
\end{bmatrix}.
\tag{5}
$$

Next, the floor contact model is elaborated.

1) Floor Contact: The ball is in floor contact if

$$
z_B \leq r_B.
\tag{6}
$$

The contact force consists of two components. $\boldsymbol{F}_{FC_n}$ is the normal force and $\boldsymbol{F}_{FC_t}$ the force tangential to the floor plane.

a) Normal force: The normal force is obtained from a Hunt–Crossley model [22] that is chosen to be

$$
\boldsymbol{F}_{FC_n} = [-K_F(z_B - r_B) - D_F(z_B - r_B)\dot{z}_B]\,\boldsymbol{e}_z
\tag{7}
$$

with $K_F = 35000 \frac{\text{N}}{\text{m}}$ being the stiffness constant and $D_F = 1600 \frac{\text{Ns}}{\text{m}}$ the damping constant.

b) Tangential force: The physical effect caused by the tangential force is that the relative velocity between ball and floor fades away over the contact. This is taken into account by a lumped LuGre model [23], being defined as

$$
\dot{s} = |\boldsymbol{v}_{FC_r}| - \frac{\sigma_0|\boldsymbol{v}_{FC_r}|}{g(\boldsymbol{v}_{FC_r})}s
\tag{8}
$$

$$
F_t = (\sigma_0 s + \sigma_1 \dot{s} + \sigma_2|\boldsymbol{v}_{FC_r}|)\,|\boldsymbol{F}_{FC_n}|
\tag{9}
$$

with

$$
g(\boldsymbol{v}_{FC_r}) = \mu_C + (\mu_s - \mu_c)e^{-|\boldsymbol{v}_{FC_r}/v_s|^\alpha}.
\tag{10}
$$

s is the slip between ball and floor, σ_0 the rubber longitudinal lumped stiffness, σ_1 the rubber longitudinal lumped damping, σ_2 the viscous relative damping, μ_c the normalized Coulomb friction, μ_s the normalized static friction, v_s the Stribeck relative velocity, F_n the normal force, and $\boldsymbol{v}_{FC_r}$ the relative velocity. The steady-state friction/slip characteristic is captured by α. In our simulations, we use following numerical values

$$
[\sigma_0 \; \sigma_1 \; \sigma_2 \; \mu_c \; \mu_s \; v_s \; \alpha]
$$
$$
= [1000 \; 1/\text{m} \; 100 \; \text{s/m} \; 0.1 \; \text{s/m} \; 0.8 \; 0.9 \; 20 \; \text{m/s} \; 1].
\tag{11}
$$

The parameters are chosen such that the friction reaches its steady state during the short floor contact time. The Coulomb friction parameters can be found in [24]. The relative velocity sought after is calculated by

$$
\boldsymbol{v}_{FC_r} = [\boldsymbol{e}_x \; \boldsymbol{e}_y \; \boldsymbol{0}]\,\dot{\boldsymbol{x}}_B + [0 \; 0 \; -r_B]^T \times \boldsymbol{\omega}_B.
\tag{12}
$$

Furthermore, (12) provides also the direction of the tangential force, as it acts in opposite direction to the relative velocity.
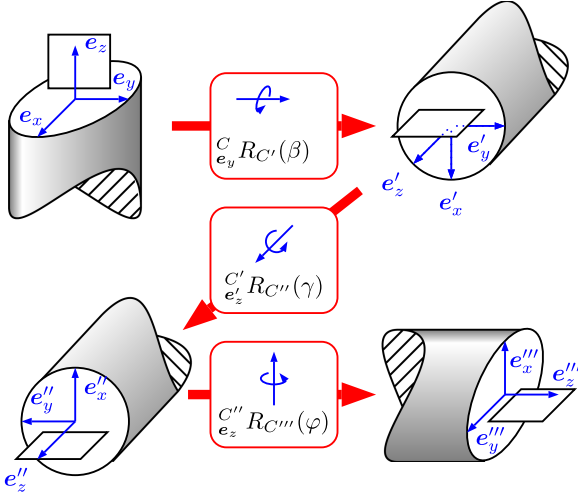
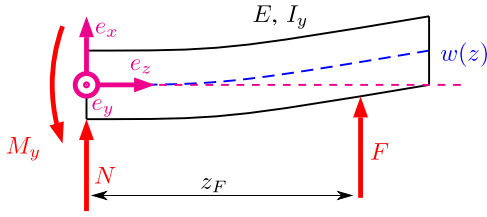Fig. 6. Rotation order for commanding the orientation of the robot hand, which is sketched as a plate.

Fig. 7. Calculation of spring stiffness K seen at the contact point.

2) Hand Model: The robot end-effector will later be commanded via a desired frame fed to a Cartesian impedance controller (see Section V). The rotation matrix is described by a well-chosen combination of relative and global angles in the sense of the task, whose rotation order is depicted in Fig. 6.

The first coordinate system $\{C\}$ is collinear to the base frame. The first rotation acts around the y-axis and is later used for controlling the ball along the d_B coordinate. Thereafter, the coordinate system is rotated around the new z-axis, which will be used for controlling the ball along the φ_B coordinate. The last rotation is around the z-axis of the base frame and is used for tracking the ball position.

3) Hand Contact: The hand contact is calculated similarly to the floor contact. Therefore, it is advantageous to use the position vector of the ball expressed in $\{EE\}$. The condition for hand contact is

$$^{EE}x_B \geq \delta_x + r_B. \tag{13}$$

We assume the absence of damping in the hand as the fingers are made of spring steel. Hence, we get

$$^{EE}\boldsymbol{F}_{HC_n} = K(\boldsymbol{x}_B, E, I_y)(-^{EE}x_B + \delta_x + r_B)^{EE}\boldsymbol{e}_x \tag{14}$$

for the normal direction of the contact.

The stiffness $K(\boldsymbol{x}_B, E, I_y)$ is calculated from the linear theory on Bernoulli beams, see Fig. 7. The force F denotes the force that is applied by the ball. This causes two reactions $M_R = F z_F$ and N, as well as the bending line $w(z)$, which is calculated

by [25]

$$EI_y \frac{\mathrm{d}^2 w(z)}{\mathrm{d}z^2} = -M_y(z). \tag{15}$$

E is the modulus of elasticity, I_y is the geometrical moment of inertia around the y-axis, and M_y is the bending moment around y, which is obtained by

$$M_y(z) = \underbrace{F z_F}_{=M_R} - \underbrace{F}_{=N} z + \begin{cases} 0, & \text{for } z \leq z_F \\ F(z - z_F), & \text{for } z > z_F \end{cases}. \tag{16}$$

Evaluating (15) at z_F results in relation (17) between the force and bending at z_F

$$F = \underbrace{\frac{EI_y}{3z_F^3}}_{K} w(z_F). \tag{17}$$

Therewith, the stiffness K seen at the contact point is known. The tangential direction of the force is calculated analog to Section II-B1 by utilizing a LuGre model. The full contact force wrench generated by the hand contact is finally denoted by $^{EE}\boldsymbol{\mathcal{F}}_{\text{ext}} = [^{EE}\boldsymbol{F}_{\text{ext}}^T \ ^{EE}\boldsymbol{M}_{\text{ext}}^T]^T$ and is explained in more detail in Section IV-D.

In this paper, we show basic simulations, which consider the robot to be a position/velocity source. However in case of the full 7-DoF analysis the according simulations and experiments take the full flexible joint dynamic model and control of a Cartesian impedance controlled robot into consideration. Therefore, we briefly introduce the underlying set of equations describing the robot dynamics next. The active impedance controller is outlined in Section IV-F.

4) Elastic Joint Robot Model: Due to the lightweight design of the LWR-III it is not sufficient to model the robot by a second-order rigid body model. The nonnegligible joint elasticity between motor and link inertia caused by the Harmonic Drive gears and the joint torque sensor has to be taken into account in the model equation. For such a robot, the flexible joint model in the form

$$M(\boldsymbol{q})\ddot{\boldsymbol{q}} + C(\boldsymbol{q}, \dot{\boldsymbol{q}})\dot{\boldsymbol{q}} + \mathbf{g}(\boldsymbol{q}) = \boldsymbol{\tau}_J + \boldsymbol{\tau}_{\text{ext}} \tag{18}$$

$$B\ddot{\boldsymbol{\theta}} + \boldsymbol{\tau}_J = \boldsymbol{\tau}_m \tag{19}$$

$$\boldsymbol{\tau}_J = K_J(\boldsymbol{\theta} - \boldsymbol{q}) \tag{20}$$

can be assumed [26] with $\boldsymbol{q}$ being the link-side position, $\boldsymbol{\theta}$ the motor position, $\boldsymbol{\tau}_J$ the elastic joint torque, $M(\boldsymbol{q})$ the mass matrix including the load of the end-effector, $C(\boldsymbol{q}, \dot{\boldsymbol{q}})\dot{\boldsymbol{q}}$ the centripetal and Coriolis vector, $\boldsymbol{g}(\boldsymbol{q})$ the gravity vector, $K_J = \text{diag}\{K_{J,i}\}$ the diagonal positive definite joint stiffness matrix, and $B = \text{diag}\{B_i\}$ the diagonal positive definite motor inertia matrix.[5] The external joint torque is generated by the ball contact wrench ideally measured in the wrist sensor via $\boldsymbol{\tau}_{\text{ext}} = J^T{}^{EE}(\boldsymbol{q})^{EE}\boldsymbol{\mathcal{F}}_{\text{ext}}$, with $J(\boldsymbol{q})$ being the $\{EE\}$ Jacobian of the manipulator. As the sensor measurement also includes a wrench resulting from gravity and the accelerated load, their

---

[5]Please note that for sake of clarity, we omit the joint damping and motor side friction. They are, however, taken into consideration in the simulation.

compensation based on an extended acceleration observer is required (see Section IV).

Now that all underlying models have been introduced, the chosen reference trajectory and an overall stability and energy analysis of the dribbling process is carried out next.

III. BASIC FEEDFORWARD CONTROL AND STABILITY ANALYSIS

For being able to analyze the stability of dribbling cycles, we introduce the chosen hand reference trajectory in this section and then deduce an analytic solution for the equation of motion for the ball in the 1-DoF case.

A. Hand Reference Trajectory for 1 DoF Model

[11] used a mirrored trajectory of the ball for robot juggling, which is essentially a parabola. Furthermore, negative acceleration seems desirable, as it was shown to lead to stable juggling cycles [13]. However, instead of a parabola we select a sinusoidal excitation motion of the hand, since during contact the considered system is modeled by a second-order mass-spring dynamic. In addition, a positive sine half-wave has also negative acceleration but changes sign at the end so that the reversal can be carried out faster. This imposes smaller velocity and acceleration requirements on the robot. Finally, a sine half-wave is a good approximation for a parabola and the hand motion of a semiprofessional human player as shown in Fig. 26 is similar to sine half-waves.

The hand trajectory in this paper is described by the three parameters amplitude A, offset z_0, and period time T. It is composed by a positive slow half-wave for $t^* \in [0, pT]$, $0.5 \leq p < 1$, and a negative fast sine half-wave for $t^* \in]pT, T[$, where

$$t^* = t - t_0 \qquad (21)$$

allows to define a time shift t_0 of the sine waves. A trajectory, which is continuous and continuously differentiable at $t = pT$ is given by

$$z(t^*) = \begin{cases} A\sin(\omega_1 t^*) + z_0, & \text{for } t^* \in [0; pT] \\ -qA\sin(\omega_2(t^* - pT)) + z_0, & \text{for } t^* \in]pT; T[\end{cases} \qquad (22)$$

where $\omega_1 = \frac{\pi}{pT}$, $\omega_2 = \frac{\pi}{(1-p)T}$, and $q = \frac{\omega_1}{\omega_2}$.

In subsequent simulations and experiments, $p = \frac{4}{5}$ and $t_0 = 0$ were chosen leading to $\omega_2(t - pT) = \frac{5\pi}{T}\left(t - \frac{4T}{5}\right) = \frac{5\pi}{T}t - 4\pi$. Thus, (22) becomes

$$z(t) = \begin{cases} A\sin\left(\frac{5\pi}{4T}t\right) + z_0, & \text{for } t \in \left[0; \frac{4}{5}T\right] \\ -\frac{1}{4}A\sin\left(\frac{5\pi}{T}t\right) + z_0, & \text{for } t \in \left]\frac{4}{5}T; T\right[\end{cases} \qquad (23)$$

which is the hand trajectory considered from now on.

In Section III-B, we derive an analytic, approximated solution for the stable cycle of the ball.

B. Analytic Solution for 1-DoF Model

Fig. 8 depicts the time instants at which the hybrid system's transitions occur. State vectors at these time instants are denoted
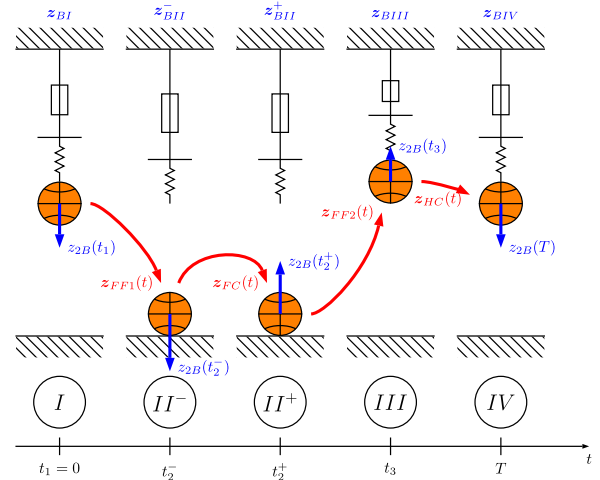

Fig. 8. State and notation conventions for the ball and hand over time are as follows. t_1, $\boldsymbol{z}_{BI}$ are the starting time and state. t_2^-, $\boldsymbol{z}_{BII}^-$ the time and state for starting floor contact, t_2^+, $\boldsymbol{z}_{BII}^+$ for the end of floor contact. t_3, $\boldsymbol{z}_{BIII}$ are the time and state at hand contact start and $t_4 = T$, $\boldsymbol{z}_{BIV}$ at its end.

with a Roman number and are depicted at the top of the figure. The timely evolution of these states between the characteristic time instants are indicated in red.

At $t_1 = 0$ s the hand contact vanishes and the initial value is $\boldsymbol{z}_{BI} := \boldsymbol{z}_B(0) = [z_{1BI}\ z_{2BI}]^T$. The velocity is defined to be negative so that the first phase of the ball is a free-flight motion.

For the free-flight phase, we get

$$\boldsymbol{z}_{FF1}(t) = \begin{bmatrix} -\frac{1}{2}gt^2 + z_{2BI}t + z_{1BI} \\ -gt + z_{2BI} \end{bmatrix}. \qquad (24)$$

The time instant t_2^- at which the ground contact occurs can be obtained by intersection of $z_{1FF1}(t)$ with the straight line $z = r_B$. We label this as the state $\boldsymbol{z}_{BII}^- := \boldsymbol{z}_{FF1}(t_2^-)$. The floor contact is then characterized by

$$\boldsymbol{z}_{BII}^+ = \begin{bmatrix} z_{1BII}^- \\ -\mathrm{COR}\, z_{2BII}^- \end{bmatrix} \qquad (25)$$

and the solution for the second free-flight phase is

$$\boldsymbol{z}_{FF2}(t) = \begin{bmatrix} -\frac{1}{2}g\left(t - t_2^+\right)^2 + z_{2BII}^+\left(t - t_2^+\right) + z_{1BII}^+ \\ -g\left(t - t_2^+\right) + z_{2BII}^+ \end{bmatrix}. \qquad (26)$$

The next time instant that has to be calculated is the start of the hand contact. This contact is assumed to occur within the slow positive half-wave of the hand trajectory. This is justified by the human motion depicted in Fig. 26, where the hand contact starts shortly before the highest hand position. As this corresponds to the intersection of a sine with a parabola no analytic solution can be provided. Therefore, we approximate the sine of the hand motion by a parabola

$$z_{\mathrm{appr}}(t) = a + b\left(t - \frac{\pi}{2\omega}\right)^2 \approx z(t) \qquad (27)$$

with $\omega = \omega_1 = \frac{\pi}{pT}$ [ref. to (22)] and the parameters a, b being selected such that they minimize the error criterion

$$J = \int_0^{\frac{\pi}{\omega}} (z_{\text{appr}} - z(t)) \, dt. \tag{28}$$

In addition, the cycle begins and consequently ends with the separation of the hand contact. Hence, the hand trajectory needs to be shifted along the time axis by t_{off} such that $z(T) = z_{1BI} + r_B$, which can be found as

$$t \leftarrow t + \underbrace{(1-p)\,T - t_0 + \frac{\arcsin\left(\frac{r_B - z_0 + z_{1L}}{A}\right)}{\omega}}_{t_{\text{off}}} \tag{29}$$

with a possible time shift t_0 of the hand trajectory introduced in (21).

With (27) both, the time t_3 and the state $\mathbf{z}_{BIII} := \mathbf{z}_{FF2}(t_3)$ are calculated. Therewith, it is possible to obtain the analytic solution for the differential (4) of the ball motion during hand contact together with the driving input, i.e., the approximated hand trajectory $z_{\text{appr}}(t)$ in (27). Within this phase, the dynamics of the ball dynamics can be written as

$$\ddot{z}_B = -g - \frac{K_H}{m_B}(z_B + r_B - z_H(t)) \tag{30}$$

where $z_H(t)$ is the hand trajectory and $K_H(z_B + r_B - z_H(t))$ the accelerating force acting on the ball, resulting from the hand stiffness K_H. The solution can be derived by splitting the input $z_H(t)$ into a constant and a time variable part and using the convolution theorem of the Laplace transform for the latter. This approach leads to

$$\mathbf{z}_{HC}(t) = \Phi \begin{bmatrix} \sin\left(\sqrt{\frac{K_H}{m_B}}(t - t_3)\right) \\ \cos\left(\sqrt{\frac{K_H}{m_B}}(t - t_3)\right) \\ \sin(\omega(t - t_3)) \\ \cos(\omega(t - t_3)) \end{bmatrix} \tag{31}$$

with

$$\Phi_{11} = z_{BIII,2}\sqrt{\frac{m_B}{K_H}} - \frac{\sqrt{K_H}\,A\omega\cos(\omega\,t_3)}{\sqrt{m_B}\left(\frac{K_H}{m_B} - \omega^2\right)}$$

$$\Phi_{12} = z_{BIII,1} + \frac{m_B g}{K_H} + r_B - z_0 - \frac{K_H A \sin(\omega\,t_3)}{m_B\left(\frac{K_H}{m_B} - \omega^2\right)}$$

$$\Phi_{13} = \frac{K_H\,A}{m_B\left(\frac{K_H}{m_B} - \omega^2\right)}, \quad \Phi_{14} = 0$$

$$\Phi_{21} = -\Phi_{12}\sqrt{\frac{K_H}{m_B}}, \quad \Phi_{22} = \Phi_{11}\sqrt{\frac{K_H}{m_B}}$$

$$\Phi_{23} = 0, \quad \Phi_{24} = \Phi_{13}g\omega.$$

With the relation $\mathbf{z}_{HC}(T) \stackrel{!}{=} \mathbf{z}_{BI}$ (where $\stackrel{!}{=}$ denotes "having to be equal to") we may inspect whether the chosen parameters result in a valid cycle. Therewith, together with the following stability analysis we are able to build regions for the set of stabilizing trajectory parameters, see Section III-E.
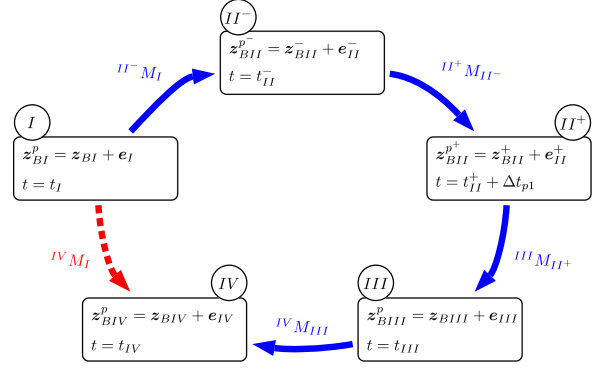

Fig. 9.   Error mapping over one dribbling cycle.

Next, let us analyze the stability of the open-loop system.

C. Limit Cycle Stability Analysis

Obviously, the system is stable for a ball lying on the floor. As we are only interested in the stability properties of dribbling limit cycles we exclude this case. The analysis of regions of attraction or stability in hybrid limit cycles is, e.g., presented in [27] and [28]. However, the approach does not lead to a stability criterion, which could be computed online and could therefore be suitable for online adaptation. Moreover, the approach is based on hybrid systems, where only the states switch at certain switching surfaces, but the system dynamics remain unchanged. In the present case, the ball dynamics are represented by ordinary differential equations varying in the three phases. These so called *hybrid systems with logical modes* are considered in [29], where a framework for showing preasymptotic stability of an equilibrium point is applied to this class of systems. Since this approach also requires a high computational effort and is not suitable for online evaluation, we develop a simpler method, which is somehow similar to [13]. First, we suppose that we have found parameters for a closed cycle according to Section II. By perturbing the initial conditions of the cycle, we elaborate a mapping of the error from the cycle start to its end. For this, we use an iterative method, which idea is summarized in Fig. 9. The desired overall mapping $^{IV}M_I$ is constructed from the concatenation of the partial mappings ^iM_j.

1) Free Flight: For free flight, we define a new perturbed initial condition

$$\mathbf{z}_{BI}^p = \mathbf{z}_{BI} + \mathbf{e}_I \tag{32}$$

where $\mathbf{e}_I = [e_{1I} \ e_{2I}]^T$ is the initial perturbation. Using the new initial condition (32) for the free flight, we obtain a perturbed state $\mathbf{z}_{BII}^{p-}$ at the nominal floor contact time t_2^-, which has the form

$$\mathbf{z}_{BII}^{p-} = \begin{bmatrix} -\frac{1}{2}g(t_2^-)^2 + (z_{2BI} + e_{2I})t_2^- + z_{1BI} + e_{1I} \\ -gt_2^- + z_{2BI} + e_{2I} \end{bmatrix}. \tag{33}$$

The influence of the perturbation $\mathbf{e}_I$ on $\mathbf{z}_{BII}^{p-}$ is linear and can already be described by a mapping matrix $^{II^-}M_I$. However, assuming small errors, our general approach implies taking a
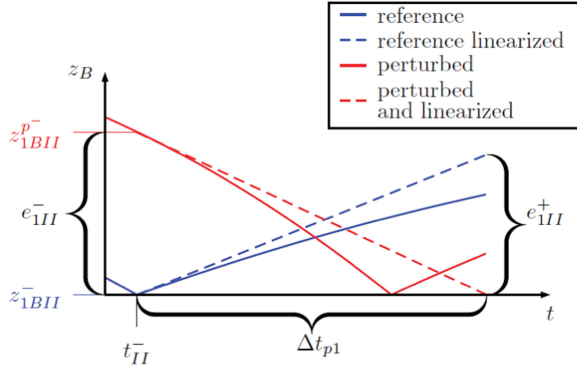
Fig. 10. Visualization of the linearized floor contact.

linearization around the nominal unperturbed solution

$$
\boldsymbol{z}_{BII}^{p^-} = \underbrace{\boldsymbol{z}_{BII}^{p^-}\Big|_{\boldsymbol{e}_I = 0}}_{\boldsymbol{z}_{BII}^-} + \underbrace{\frac{\partial \boldsymbol{z}_{BII}^{p^-}}{\partial \boldsymbol{e}_I}\Big|_{\boldsymbol{e}_I = 0}}_{=:^{II^-} M_I} \boldsymbol{e}_I
$$

$$
= \boldsymbol{z}_{BII}^- + \boldsymbol{e}_{II}^-. \tag{34}
$$

The matrix $^{II^-} M_I$ thereby maps the error $\boldsymbol{e}_I$ at t_1 to the error $\boldsymbol{e}_{II}^-$ at t_2^- and is found to be

$$
^{II^-} M_I = \begin{bmatrix} 1 & t_2^- \\ 0 & 1 \end{bmatrix}. \tag{35}
$$

2) Floor Contact: Since the nominal contact time is not the real one anymore, we have to calculate the perturbed contact time. As we assume small errors, the first-order approximation of the perturbed analytic solution

$$
\boldsymbol{z}_{FF1}^{p^{\text{lin}}}(t) = \begin{bmatrix} z_{2BII}^{p^-} t + z_{1BII}^{p^-} \\ z_{2BII}^{p^-} \end{bmatrix} \tag{36}
$$

may be taken at the nominal contact time t_2^-. The time offset Δt_{p1} is then calculated by intersection with the floor

$$
z_{1FF1}^{p^{\text{lin}}}(\Delta t_{p1}) \stackrel{!}{=} r_B. \tag{37}
$$

The error after this small time offset Δt_{p1} is calculated by the difference of the first-order approximation of the nominal solution after floor contact $\boldsymbol{z}_{FF2}^{\text{lin}}(t)$ and the first-order approximation of the perturbed solution $\boldsymbol{z}_{FF1}^{p^{\text{lin}}}(t)$. This yields the error of the perturbed trajectory after the floor contact (see Fig. 10)

$$
\boldsymbol{e}_{II}^+ = \boldsymbol{z}_{FF2}^{\text{lin}}(\Delta t_{p1}) - \boldsymbol{z}_{FF1}^{p^{\text{lin}}}(\Delta t_{p1})
$$

$$
= \begin{bmatrix} z_{2BII}^+ \Delta t_{p1} + z_{1BII}^+ \\ z_{2BII}^+ \end{bmatrix} - \begin{bmatrix} z_{2BII}^{p^-} \Delta t_{p1} + z_{1BII}^{p^-} \\ -\text{COR} z_{2BII}^{p^-} \end{bmatrix}. \tag{38}
$$

We obtain for this error the linearization around $\boldsymbol{e}_{II}^- = \boldsymbol{0}$

$$
\boldsymbol{e}_{II}^{+^{\text{lin}}} = \underbrace{\boldsymbol{e}_{II}^+\Big|_{\boldsymbol{e}_{II}^- = \boldsymbol{0}}}_{=\boldsymbol{0}} + \underbrace{\frac{\partial \boldsymbol{e}_{II}^+}{\partial \boldsymbol{e}_{II}^-}\Big|_{\boldsymbol{e}_{II}^- = \boldsymbol{0}}}_{=^{II^+} M_{II^-}} \boldsymbol{e}_{II}^- \tag{39}
$$

with the error mapping matrix

$$
^{II^+} M_{II^-} = \begin{bmatrix} -1 & 0 \\ 0 & \text{COR} \end{bmatrix}. \tag{40}
$$

3) Free Flight: The second free-flight phase is calculated from the time instant of the perturbed floor contact $t_2^- + \Delta t_{p1}$. Therefore, we take a new initial condition for the free flight as

$$
\boldsymbol{z}_{BII}^{p^+} = \boldsymbol{z}_{FF2}(t_2^- + \Delta t_{p1}) + \boldsymbol{e}_{II}^{+^{\text{lin}}}. \tag{41}
$$

In the second free-flight phase, we get the same mapping as for the first free-flight phase, see Section III-C1. This yields

$$
\boldsymbol{z}_{BIII}^p = \underbrace{\boldsymbol{z}_{BIII}^p\Big|_{\boldsymbol{e}_{BII}^+ = \boldsymbol{0}}}_{\boldsymbol{z}_{BIII}} + \underbrace{\frac{\partial \boldsymbol{z}_{BIII}^p}{\partial \boldsymbol{e}_{BII}^+}\Big|_{\boldsymbol{e}_{BII}^+ = \boldsymbol{0}}}_{=:^{III} M_{II^+}} \boldsymbol{e}_{II}^{+^{\text{lin}}}
$$

$$
=: \boldsymbol{z}_{BIII} + \boldsymbol{e}_{III}. \tag{42}
$$

The transition matrix is therefore

$$
^{III} M_{II^+} = \begin{bmatrix} 1 & t_3 - t_2^- \\ 0 & 1 \end{bmatrix}. \tag{43}
$$

With the argument from Section III-C2, a new intersection point of the hand trajectory with the ball trajectory needs to be calculated. However, this case is already included in (43), as only a negligible time increment would be added in element $\{1, 2\}$ of the matrix $^{III} M_{II^+}$ in (43).

4) Hand Contact: The approximation of the error propagation during hand contact follows the scheme already presented for the previous phases. By inserting the perturbed initial conditions $\boldsymbol{z}_{BIII}^p = \boldsymbol{z}_{BIII} + \boldsymbol{e}_{III}$ from (42) at t_3 into Φ_{11} and Φ_{12} in (31) we obtain the perturbed solution for the hand contact. Then, the linearization around $\boldsymbol{e}_{III} = \boldsymbol{0}$ at t_4 yields

$$
^{IV} M_{III} = \begin{bmatrix} \cos(c\Delta t) & \frac{1}{c}\sin(c\Delta t) \\ -c\sin(c\Delta t) & \cos(c\Delta t) \end{bmatrix} \tag{44}
$$

with $\Delta t = t_4 - t_3 = T - t_3$ and $c = \sqrt{K_H / m_B}$.

5) Total Error Propagation: Combining (35), (40), (43), and (44), we construct the mapping of the error $\boldsymbol{e}_{I_n}$ of cycle n to the initial error $\boldsymbol{e}_{I_{n+1}}$ of the next cycle $n + 1$ by multiplication of the error mapping matrices. This yields to the difference equation

$$
\boldsymbol{e}_{I_{n+1}} = \underbrace{^{IV} M_{III}\ {}^{III} M_{II^+}\ {}^{II^+} M_{II^-}\ {}^{II^-} M_I}_{^{IV} M_I} \boldsymbol{e}_{I_n}. \tag{45}
$$

By analyzing whether the absolute value of the eigenvalues of the matrix $^{IV} M_I$ remains below 1, we can conclude the stability of the cycle. The eigenvalues also provide an approximation of the convergence rate of the system.
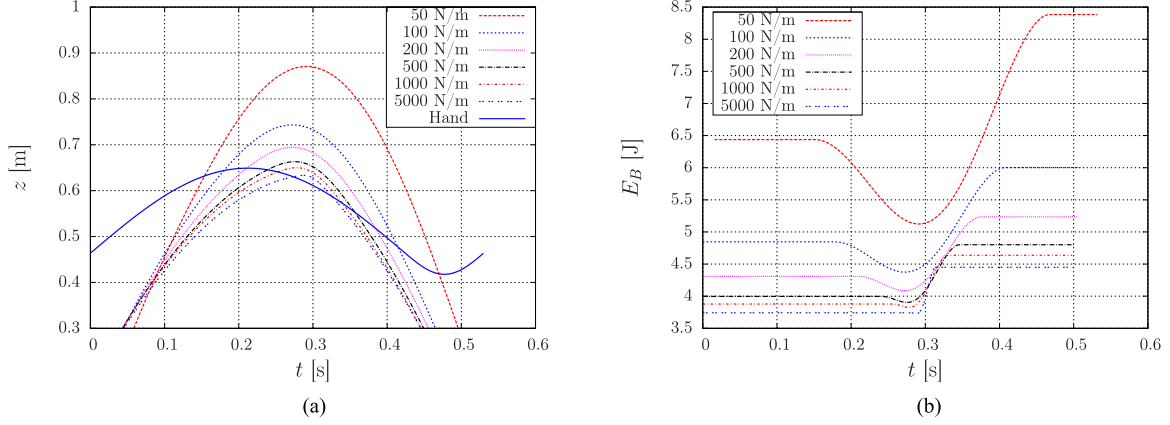
Fig. 11. Ball trajectory (a) and energy (b) for different hand stiffnesses at constant excitation motion. (a) Dribbling cycle for the same hand trajectory with different hand stiffnesses. (b) Energy for one cycle and different hand stiffnesses.

D. Energy-Based Analysis

Apart from achieving a stable dribbling motion the question that hand stiffness should be used ideally in order to minimize peak power or increase robustness of the cycle is worth to be investigated. The last aspect is especially important for real robots, which are generally deviating from the desired motion (in particular for such highly dynamic motions). This is particularly true for impedance controlled robots [15].

In order to analyze the effect of different hand stiffnesses, we take a closer look at the system with the trajectory used later in simulations (see Section IV-C) and varying hand stiffnesses. In Fig. 11(a), we find the ball position for varying stiffnesses over one cycle beginning and ending at the floor contact (after the system has already reached a stable cycle over time). The used hand trajectory is defined by $A = 0.17$ m, $z_0 = 0.6$ m, and $T = 0.52$ s.[6] Obviously, increasing hand stiffness leads to a decreasing apex height and therewith, also to a decrease in energy level, see Fig. 11(b). As expected, the contact time increases with decreasing stiffness. This is a significant benefit one obtains from the elastic properties: more time to control the robot during hand contact.[7] The experimental performance of this approach can be found in [15].

Interesting to notice is the energetic system behavior in terms of energy flow. We therefore consider a system, which border corresponds to the spring bearing. Hence, we obtain two energy tanks in the system. One energy portion E_B is stored in the ball, consisting of its potential and kinetic energy. The second one is stored in the spring as potential energy E_S, see Fig. 12 (the energy flow is also depicted). Generally, there are two energy flows: 1) $\dot{E}_{BS}$ between the two storage devices ball and spring, and 2) W_S, which is the work originating from outside the system (i.e., the robot) and acts on the spring.
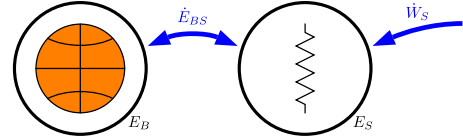

Fig. 12. Energy flow of a system consisting of a ball and a spring.

Hence, we can write the overall system energy balance as

$$E_B(t) + E_S(t) - E_0 = \int_{t_0}^{t} \dot{W}_S(t)\mathrm{d}t = W_S(t) \tag{46}$$

$$E_B(t) = m_B g z_B(t) + \frac{1}{2} m_B \dot{z}_B(t)^2 \tag{47}$$

$$E_S(t) = \begin{cases} \frac{1}{2} K_H (z(t) - z_B(t) - r_B)^2, & z(t) < z_B(t) + r_B \\ 0, & z(t) > z_B(t) + r_B \end{cases} \tag{48}$$

for calculating the work to be put into the system. E_0 denotes the initial energy already stored in the system at $t = t_0$.

The work W_S is shown in Fig. 13(a). An interesting aspect is that for small stiffnesses the energy flows first out of the system before rising. This is due to the initial upwards hand motion at the start of the hand contact [see Fig 11(a)], which extracts potential energy from the system. Knowing the work of the system, we may obtain the power

$$P_s = \dot{W}_s \tag{49}$$

that flows into the system. The power flow for the different stiffnesses is depicted in Fig. 13(b). It is obvious by looking at the apexes of the curves that a stiffness with minimal power consumption exists. This property is depicted in Fig. 14. Looking at the relation between power apex and hand spring stiffness, it is clear that an optimal hand stiffness can be selected that leads to a minimum power consumption for a given trajectory.

E. Stability Considerations for Varying Hand Stiffness

Apart from the preceding energy and power analysis, we investigate which hand trajectories lead to a stable periodic cycle

---

[6]Please note that in Fig. 11 the hand trajectory is displaced by $-r_B = -0.121$ m, i.e., start and end times of the hand-ball contacts are given by the intersections of hand and ball trajectories.

[7]Please note that, due to the resulting large deformations, the simulated trajectories with very small stiffnesses might not be carried out on the real robot.
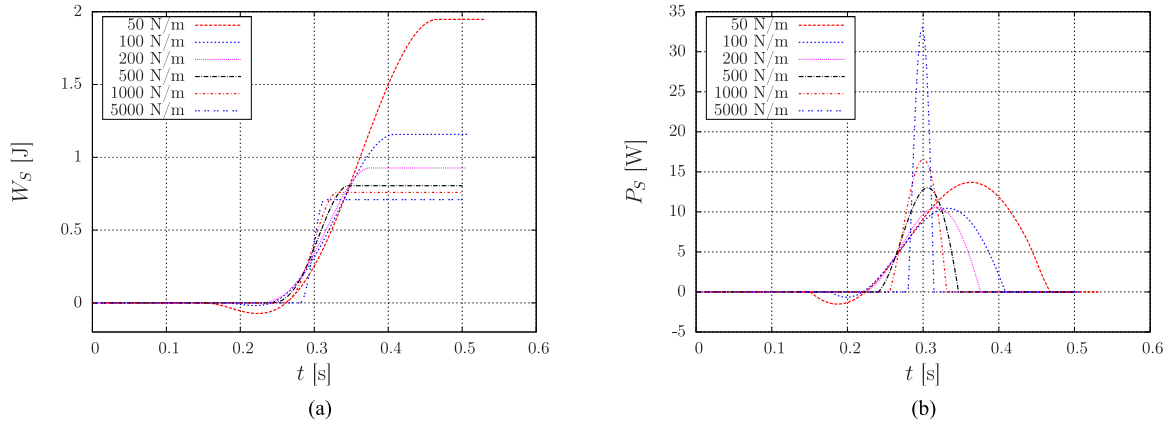
Fig. 13. Work W_S (a) and power P_S (b) for the dribbling cycle with varying hand stiffnesses. (a) Work for one cycle and different stiffnesses. (b) Power for one cycle and different stiffnesses.
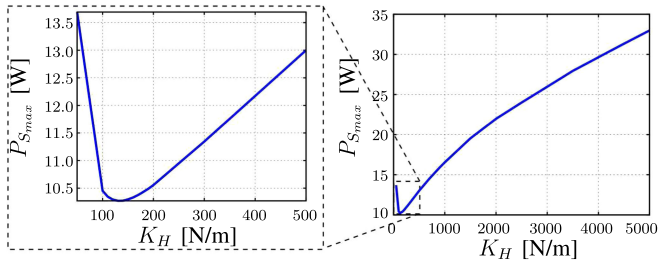
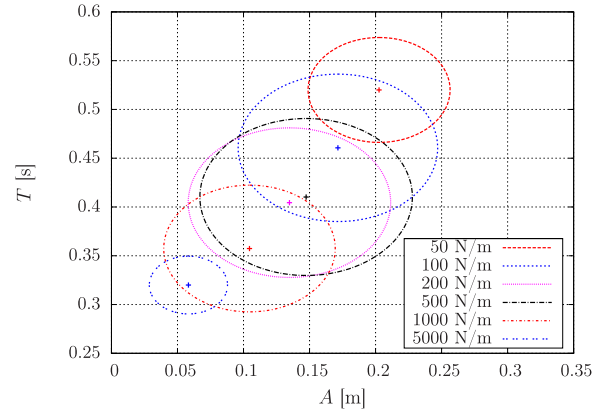

Fig. 14. Power as a function of hand stiffness K_H

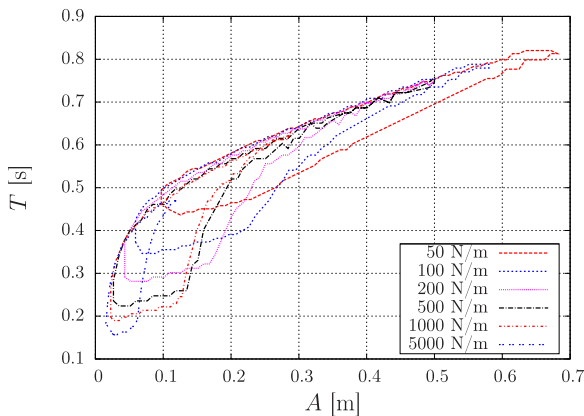Fig. 15. Areas with stable cycles for different stiffnesses.

Fig. 16. Inscribed circles of the areas with stable cycles for different stiffnesses.

area when considering real robotic systems, which can suffer nonnegligible tracking and sensor errors.

Table I summarizes the aforementioned results for the given example. It lists the position (A_C and T_C) and radius r_c of the circle, the maximal robot velocity $\dot{z}_{C_{\max}}$ and acceleration $\ddot{z}_{C_{\max}}$ (resulting from the center of the circle), and the maximal power $P_{\max}$ and force $F_{\max}$ for the cycles from Fig. 11(a) in case of different stiffnesses. Clearly, the second large benefit of intrinsically elastic robots becomes clear: The significant reduction of contact forces, which leads to a load reduction for the physical robot.

Until now, the trajectory height z_0 remained the same. We examined mainly the case of dribbling at a given height. Another interesting aspect is the dribbling at a desired ball energy level that is related to the ball height and velocity. Fig. 17(a) shows two ball trajectories for a cycle that starts on the same energy level but with different stiffnesses. Clearly, we need a significantly faster hand trajectory for the high stiffness case compared to an elastic (compliant) robot.

In the following section, a nonlinear hybrid observer is designed that enables the robot to provide stable tracking and

and their relation to hand stiffness. Fig. 15 depicts the simulation analysis results for varying A, T, and K_H at constant height z_0. The stability check for obtaining the plotted regions was done by applying the equations for the periodic cycle of Section III-B and the according stability analysis from Section III-C. For higher hand stiffnesses, we generally need smaller amplitudes and period times.

As the areas from Fig. 15 are not uniquely comparable w.r.t. their size and position, we inscribe a circle in each region, see Fig. 16. These circles can be interpreted as a robustness

TABLE I
COMPARISON

| K_H [N/m]	A_C [m]	T_C [s]	f_C [Hz]	r_C	$\dot{z}_{C_{\max}}$ [m/s]	$\ddot{z}_{C_{\max}}$ [m/s^2]	$P_{\max}$ [W]	$F_{\max}$ [N]
50	0.2027	0.5200	2.4040	0.0538	1.5305	11.5590	13.6918	12.7022
100	0.1715	0.4606	2.7137	0.0756	1.4617	12.4620	10.4531	11.4802
200	0.1348	0.4045	3.0905	0.0767	1.3086	12.70533	10.5489	12.8450
500	0.1474	0.4102	3.0470	0.0805	1.4113	13.5093	12.9995	17.0401
1000	0.1045	0.3574	3.4972	0.0650	1.1485	12.6185	16.5415	22.2808
5000	0.0583	0.3200	3.9066	0.0296	0.7153	8.7794	32.9895	44.7021
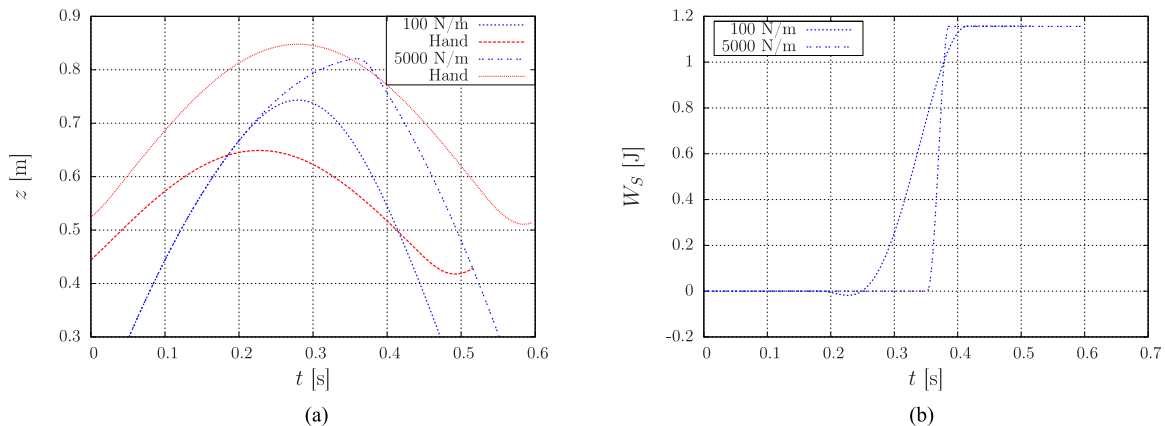
Fig. 17. Dribbling at the same energy level with two different hand stiffnesses. (a) Shows the position of hand and ball. (b) Depicts the energy trajectory for both systems.

prediction of the ball trajectory with contact force information only and does not require additional visual information. Furthermore, we outline how to control the ball with this additional information for achieving a robust dribbling cycle.

IV. BALL OBSERVER AND REFERENCE CONTROL

As outlined in the previous section, intrinsically stable dribbling cycles are achievable. However, in reality possibly significant process uncertainties may lead to their deterioration easily. Thus, reliable estimation of the ball state by suitable observers also during the free-flight phase is required allowing a practical predictive control law that compensates for these uncertainties actively.

A. Ball Observer for the 1-DoF Model

In order to solve the aforementioned problem of tracking the ball trajectory with proprioceptive sensing only, we use a nonlinear observer. For this observer scheme, we then provide a stability proof over the full cycle, for which we assume that the ball is initially in contact with the elasticity (otherwise the system is not maintaining a stable cycle and no measurement would be available).

Since we are only measuring the forces acting during the contact phase, we lack a continuous measurement. Hence, we require an observer that converges in finite time during the contact phase. A sliding mode observer is proposed in [30] that satisfies our requirement. Given a general autonomous

nonlinear system of the form

$$\dot{\boldsymbol{x}} = \boldsymbol{f}(\boldsymbol{x}), \ \boldsymbol{x} \in \mathbb{R}^n$$
$$y = h(\boldsymbol{x}), \ y \in \mathbb{R}. \tag{50}$$

In (50), $\boldsymbol{u}$ (the input) is dropped for simplicity. The observer for such a system is defined as

$$\dot{\hat{\boldsymbol{x}}} = \left(\frac{\partial \boldsymbol{H}(\hat{\boldsymbol{x}})}{\partial \boldsymbol{x}} \right)^{-1} M(\hat{\boldsymbol{x}}) \mathrm{sgn}(\boldsymbol{V}(t) - \boldsymbol{H}(\hat{\boldsymbol{x}})) \tag{51}$$

with

$$\boldsymbol{H}(\boldsymbol{x}) = [h(\boldsymbol{x}) \ L_{\boldsymbol{f}} h(\boldsymbol{x}) \ \dots \ L_{\boldsymbol{f}}^{n-1} h(\boldsymbol{x})]^T$$
$$M(\hat{\boldsymbol{x}}) = \mathrm{diag}(m_1(\hat{\boldsymbol{x}}) \ \dots \ m_n(\hat{\boldsymbol{x}}))$$
$$\boldsymbol{V}(t) = [v_1(t) \ \dots \ v_n(t)]^T. \tag{52}$$

The coefficients v_i result from the available measurement and are defined as

$$v_1 = y(t)$$
$$v_{i+1} = m_i(\hat{\boldsymbol{x}}) \mathrm{sgn}(v_i(t) - h_i(\hat{\boldsymbol{x}})), \ i = 1(1)n - 1. \tag{53}$$

Drakunov [30] provides a proof that the observer converges for bounded errors in finite time depending on the gain matrix $M(\hat{\boldsymbol{x}})$. With the force acting on the robot hand, its position and the known spring stiffness of the hand we calculate the ball position and obtain the quantity y_B that acts as the observer
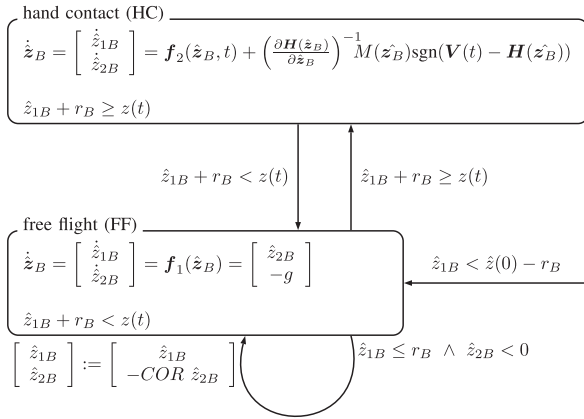
Fig. 18. Directed graph of the ball observer.

input

$$y_B(t) = \frac{F}{K_H} - r_B + z(t) \qquad (54)$$

with F being the measured force. Therewith, the observer equation during hand contact is

$$\dot{\hat{\boldsymbol{z}}}_B = \boldsymbol{f}_2(\hat{\boldsymbol{z}}_B, t) + \left(\frac{\partial \boldsymbol{H}(\hat{\boldsymbol{z}}_B)}{\partial \hat{\boldsymbol{z}}_B}\right)^{-1} M(\hat{\boldsymbol{z}}_B)\mathrm{sgn}(\boldsymbol{V}(t) - \boldsymbol{H}(\hat{\boldsymbol{z}}_B)) \qquad (55)$$

where $\boldsymbol{f}_i(\hat{\boldsymbol{z}}_B, t)$, $(i = 2)$ is the system function of the ball dynamics during the respective phase (here hand contact). For the ball being in the free-flight phase, we use a prediction step based on the model equations shown in Fig. 3. The overall hybrid observer structure, represented as a directed graph is depicted in Fig. 18.

In Section IV-B, we give a stability analysis of the hybrid observer for the entire dribbling cycle based on the Lyapunov stability definition (up to now only the convergence during contact phase is available).

B. Stability Proof for the 1-DoF Observer

As the sliding mode observer provides convergence for bounded errors in finite time depending on the chosen gain matrix, there is no general need for a stability proof. However, as the observer converges with a constant slope, it needs to be proven that during the unobserved part the observer remains within a bounded region.

For this we consider the typical ε, δ definition of Lyapunov stability that can be found in every standard nonlinear control textbook (e.g., [31]).

Definition 1 (Lyapunov stability cf., [31]). The equilibrium point $\boldsymbol{x} = 0$ of (50) is
1) stable if, for each $\varepsilon > 0$, there is $\delta = \delta(\varepsilon) > 0$ such that

$$||\boldsymbol{x}(0)|| < \delta \Rightarrow ||\boldsymbol{x}(t)|| < \varepsilon \quad \forall\, t \geq 0. \qquad (56)$$

In the following, we analyze only the time before hand contact, as the sliding mode observer itself is stable. The idea is to show the boundedness of the error mapping during

noncontact phase. For this we construct the ε, δ bounds that directly represent definition 1.

As we treat a linear system only, we may refer to the analysis from Section III-C1 to Section III-C3 for the evaluation of observer error dynamics. First, we obtain a mapping from the initial error (ball leaves hand contact) to the error at the start of the next hand contact by calculating

$$\boldsymbol{e}_{III} = \underbrace{{}^{III}M_{II^+}\;{}^{II^+}M_{II^-}\;{}^{II^-}M_I}_{{}^{III}M_I}\,\boldsymbol{e}_I. \qquad (57)$$

This results in

$$^{III}M_I = \begin{bmatrix} -1 & -COR\,t_3 \\ 0 & -COR \end{bmatrix}. \qquad (58)$$

Our interest in (58) is the mapping of balls at t_3 (beginning of next hand contact) defined as

$$B_{III} = \{\boldsymbol{e}_{III} \in \mathbb{R}^2 \mid ||\boldsymbol{e}_{III}||_2 < \varepsilon\} \qquad (59)$$

back to t_1 (ball leaves previous hand contact). Let us analyze the mapping of the border of B_{III} to t_1 by building the scalar product of $\boldsymbol{e}_{III}$ with itself, defining that B_{III} is the border of $\boldsymbol{e}_{III}$. This yields to

$$\boldsymbol{e}_{III}^T \boldsymbol{e}_{III} = \boldsymbol{e}_I^T\;{}^{III}M_I^T\;{}^{III}M_I\,\boldsymbol{e}_I = \varepsilon^2$$
$$\Leftrightarrow \boldsymbol{e}_I^T \begin{bmatrix} 1 & COR\,t_3 \\ COR\,t_3 & COR^2(1 + t_3^2) \end{bmatrix} \boldsymbol{e}_I = \varepsilon^2. \qquad (60)$$

Equation (60) corresponds to a quadric that can be transformed by a main axis transformation to an ellipse E_I of the form

$$\boldsymbol{e}_I^T \begin{bmatrix} \dfrac{1}{\varepsilon^2 a_1^2(COR, t_3)} & 0 \\ 0 & \dfrac{1}{\varepsilon^2 a_2^2(COR, t_3)} \end{bmatrix} \boldsymbol{e}_I = 1 \qquad (61)$$

where εa_1 and εa_2 are the lengths of the semiaxes of the ellipse. Without loss of generality let εa_1 denote the smaller semiaxis. Therewith, we can define a ball at t_1 with

$$B_I = \{\boldsymbol{e}_I \in \mathbb{R}^2 \mid ||\boldsymbol{e}_I||_2 < \varepsilon a_1\} \qquad (62)$$

which is a region at t_1. By mapping this circle back to t_3 via ${}^I M_{III}$, we construct an ellipse that lies inside B_{III}. This curve has two contact points at the major semiaxis. By taking the open set from B_{III} as ε and the open set from B_I as δ we get the function

$$\delta(\varepsilon) = \varepsilon a_1. \qquad (63)$$

This approach is valid, as the region of the open set for B_I is a subset of the obtained ellipse from the first mapping of B_{III}. Furthermore, the open set resulting from the mapping from B_I forward is also a subset of B_{III}. Therefore, the system is stable.

Fig. 19 illustrates this approach. The left image shows the region of the circle B_{III}. For the given example, we choose $\varepsilon = 1$. By mapping this region forward via ${}^{III}M_I$, we obtain the black ellipse E_I (middle plot). The blue and red circle B_I is the inscribed circle of the ellipse and represents δ. By mapping
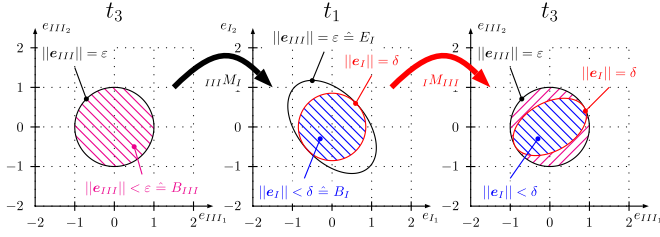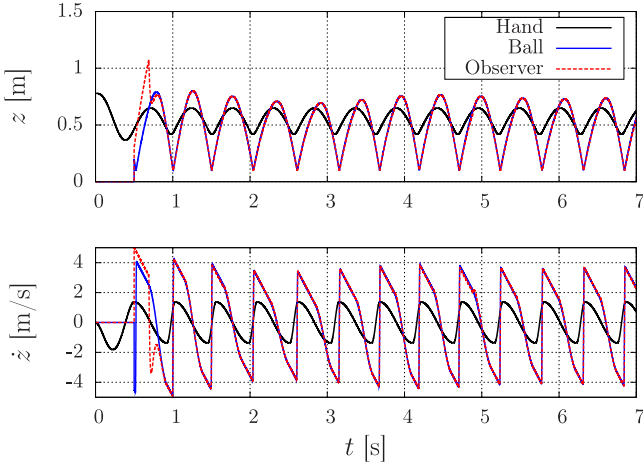
Fig. 19. ε and δ regions for the proposed observer.

Fig. 20.   Position and velocity for a sample dribbling simulation.

this via $^{I}M_{III}$, we obtain the red and blue ellipse (right plot). Finally, the downwards hatched, blue region lies completely in the black circle, which represents ε.

C. Simulation Results for 1-DoF Case

A sample simulation is shown in Fig. 20. The black line depicts the hand trajectory z, which is shifted by an offset $-r_B$. For $t \leq 0.5$ s, we simply use a fifth-order polynomial to reach the stimulating trajectory (23). The blue curve depicts the ball motion z_B. It starts for $t > 0.5$ s. From the apex heights it becomes clear that the ball stabilizes its height after some cycles. The dashed red plot denotes the ball observer position $\hat{z}_B$. Its initial position is set to the ball position, while its velocity has a significantly larger value than the true ball velocity. Despite this large initial discrepancy, it can be seen that the observer converges during the first contact phase and subsequently tracks the ball accurately. Next, the ball observer is extended to track a ball in full task dimensionality.

D. Ball Observer for the 6-DoF Model

As shown already, a sliding mode observer can be used for the estimation of the vertical ball motion. The other translations x_B and y_B can be observed with the help of a similar scheme. As for the 1-DoF problem the sliding mode observer [30] is responsible during hand contact and a model-based prediction covers the remaining noncontact phase. The observer input is the ball position obtained from measured wrenches in the wrist frame only (end-effector frame). Since we assume negligible

contact moments, we can use the principle of solidification for calculating the ball position, i.e., there has to be a straight line on which only forces but no moments are acting [32]. This straight line is the set of all points $^{EE}\boldsymbol{r}_S(\lambda)$, with λ being the curve parameter, where $^{EE}\boldsymbol{F}_{\text{ext}}$ may act in order to lead to $^{EE}\boldsymbol{M}_{\text{ext}}$ at the sensor. Consequently, all position vectors $^{EE}\boldsymbol{r}_S(\lambda)$ are valid lever arms that can be found by solving

$$^{EE}\boldsymbol{M}_{\text{ext}} = {}^{EE}\boldsymbol{r}_S(\lambda) \times {}^{EE}\boldsymbol{F}_{\text{ext}} \tag{64}$$

for $^{EE}\boldsymbol{r}_S(\lambda)$, with λ being the curve parameter of the straight line. Therewith, the contact point $^{EE}\boldsymbol{r}_C$ between ball and hand is obtained from the intersection of $^{EE}\boldsymbol{r}_S(\lambda)$ with the finger plane $^{EE}x = -\delta_x$. With $^{EE}\boldsymbol{r}_C$ and (17) we obtain the stiffness at the point of contact. Hence, with the direction of the straight line, which is given by $^{EE}\boldsymbol{F}_{\text{ext}}$ itself, we get the ball position as

$$^{EE}\boldsymbol{r}_B = {}^{EE}\boldsymbol{r}_C + \frac{{}^{EE}\boldsymbol{F}_{\text{ext}}}{|{}^{EE}\boldsymbol{F}_{\text{ext}}|} \left(-r_B + \frac{|{}^{EE}\boldsymbol{F}_{\text{ext}}|}{K({}^{EE}\boldsymbol{r}_C, E, I_y)} \right). \tag{65}$$

Equation (65) takes the ball radius r_B and the spring bending into account. As the sliding mode observer tends to scattering, we filter the observed ball position with a third-order delay element prior to using it in the feedback loop (see Section IV-E). Therewith, we get a reference that is three-times continuously differentiable, i.e., only jerk scatters.

The required contact force $^{EE}\boldsymbol{F}_{\text{ext}}$ is measured by a force sensor. However, the sensor signal contains not only contact forces, but also high-frequency noise, disturbances due to the oscillations of the intrinsically compliant fingers and most notably gravity and inertial effects of the load that are seen by the sensor while performing the dribbling motion. Therefore, we need to compensate the most significant effects for reliably estimating the contact point of the ball. In order to eliminate the high-frequency noise, we simply filter the raw signal with a second-order delay element. Finger oscillations have small amplitude and the associated frequency is very close to the frequency spectrum of the contact force. Thus, we neglect this effect. Because the desired dribbling motion demands very high acceleration, inertial forces due to the load mass are the most significant disturbance. Since acceleration cannot be obtained from currently available position sensors via twice numerical differentiation, an appropriate method to observe the operational space acceleration of the robot flange is required.

For this, the nonlinear disturbance observer from [33], which is defined as

$$\hat{\ddot{\boldsymbol{q}}} = \hat{M}^{-1}(\boldsymbol{q})(\boldsymbol{\tau} - \hat{\boldsymbol{n}}(\boldsymbol{q}, \dot{\boldsymbol{q}}) - K_O(\hat{\dot{\boldsymbol{q}}} - \dot{\boldsymbol{q}})) \tag{66}$$

is extended. In this observer, $\hat{\dot{\boldsymbol{q}}}$ denotes the observed joint velocity, $\hat{\boldsymbol{n}}(\boldsymbol{q}, \dot{\boldsymbol{q}}) = \hat{C}(\boldsymbol{q}, \dot{\boldsymbol{q}})\dot{\boldsymbol{q}} + \hat{\boldsymbol{g}}(\boldsymbol{q})$, $K_O = \text{diag}\{k_{oi} > 0\}$, $i = 1, ..., n$ is the observer gain matrix and $\{\hat{M}(\boldsymbol{q}), \hat{C}(\boldsymbol{q}, \dot{\boldsymbol{q}}), \hat{\boldsymbol{g}}(\boldsymbol{q})\}$ are the estimated robot dynamics including the load of the end-effector. The torque $\boldsymbol{\tau}$ denotes the motor joint torque in case of rigid dynamics and the elastic joint torque $\boldsymbol{\tau}_J$ in the flexible joint case. With this, an observation $\hat{\ddot{\boldsymbol{q}}}$ of $\ddot{\boldsymbol{q}}$ that relies on the measurement of joint position and velocity, as well as joint torque only is obtained. The dashed upper frame in Fig. 21 depicts the
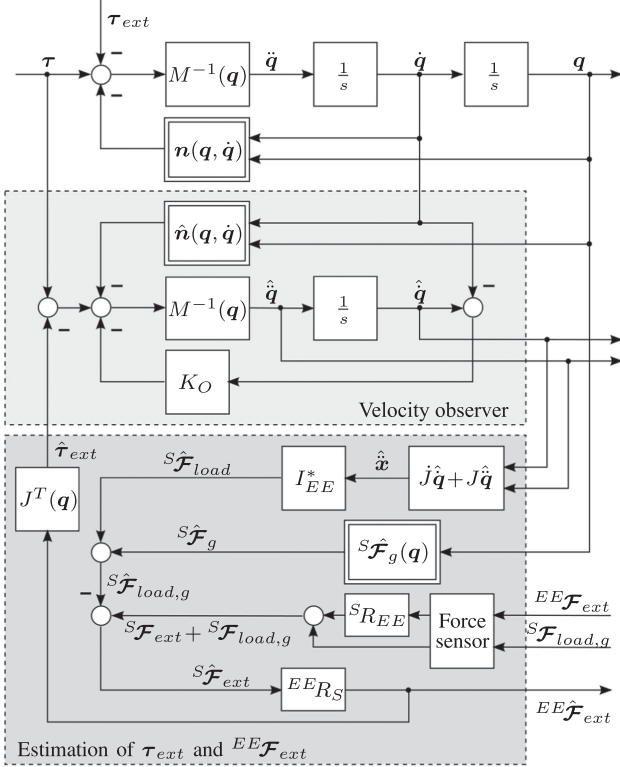
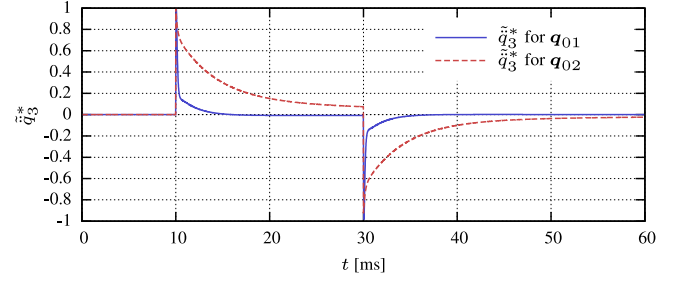Fig. 21. Extended velocity disturbance observer.

Fig. 22. Normalized observer error $\tilde{\ddot{q}}_3^*$ for the acceleration in axis 3 in relation to its maximal absolute value (denoted by *); external wrench $^{EE}\mathcal{F}_{\text{ext}} = (20\,\text{N},\ 10\,\text{N},\ 0,\ 0,\ 0,\ 0)^T$ for $10 \leq t \leq 30$ ms, $k_{O,i} = 50$ s^{-1}, $\boldsymbol{q}_{01} = (0,\ 0,\ 0,\ 0,\ 0,\ 0,\ 0)^T$ rad and $\boldsymbol{q}_{02} = (0,\ 1.3,\ 0,\ 1.3,\ 0,\ 1,\ 0)^T$ rad.

The stability of the observer error can be proven by a linear transform of $\boldsymbol{e}$

$$\bar{\boldsymbol{e}} : = K_O^{\frac{1}{2}} \boldsymbol{e} \quad \Leftrightarrow \quad \boldsymbol{e} = K_O^{-\frac{1}{2}} \bar{\boldsymbol{e}} \tag{71}$$

$$\dot{\bar{\boldsymbol{e}}} = K_O^{\frac{1}{2}} \dot{\boldsymbol{e}} = -K_O^{\frac{1}{2}} M^{-1}(\boldsymbol{q}) K_O \boldsymbol{e} - K_O^{\frac{1}{2}} M^{-1}(\boldsymbol{q}) \boldsymbol{\tau}_{\text{ext}} \tag{72}$$

$$= -K_O^{\frac{1}{2}} M^{-1}(\boldsymbol{q}) K_O^{\frac{1}{2}} \bar{\boldsymbol{e}} - K_O^{\frac{1}{2}} M^{-1}(\boldsymbol{q}) \boldsymbol{\tau}_{\text{ext}} \tag{73}$$

with $K_O^{\frac{1}{2}} = \text{diag}\left\{\sqrt{k_{O,i}} > 0\right\}$ being nonsingular and symmetric. Since $M(\boldsymbol{q})$ and $M^{-1}(\boldsymbol{q})$ are symmetric and positive definite, it follows from [35, Th. C.4] that $K_O^{\frac{1}{2}} M^{-1}(\boldsymbol{q}) K_O^{\frac{1}{2}}$ is also symmetric and positive definite. The Lyapunov function $V = \bar{\boldsymbol{e}}^T Q \bar{\boldsymbol{e}}$ with a symmetric, positive matrix Q, $\boldsymbol{\tau}_{\text{ext}} = \boldsymbol{0}$, and $\bar{A} = \bar{A}^T = -K_O^{\frac{1}{2}} M^{-1}(\boldsymbol{q}) K_O^{\frac{1}{2}}$ results in

$$\dot{V} = \dot{\bar{\boldsymbol{e}}}^T Q \bar{\boldsymbol{e}} + \bar{\boldsymbol{e}}^T Q \dot{\bar{\boldsymbol{e}}} = \bar{\boldsymbol{e}}^T \left(\bar{A}^T Q + Q \bar{A} \right) \bar{\boldsymbol{e}}. \tag{74}$$

Selecting Q to be the identity matrix, the remaining system matrix

$$\bar{A}^T + \bar{A} = 2\bar{A} = -2 K_O^{\frac{1}{2}} M^{-1} K_O^{\frac{1}{2}} \tag{75}$$

of the observer error dynamics is negative definite and the observer error is asymptotically stable.

The influence of $M(\boldsymbol{q})$ on $\boldsymbol{e}$ is demonstrated by the following exemplary simulation. Fig. 22 depicts the results for the acceleration error $\tilde{\ddot{q}}_3^*$ in axis 3 of the LWR (normalized with respect to its absolute maximum) with observer gains $k_{O,i} = 5$ and the presence of unknown external torques caused by $^{EE}\mathcal{F}_{\text{ext}} = (20\,\text{N},\ 10\,\text{N},\ 0,\ 0,\ 0,\ 0)^T$ for $10\,\text{ms} \leq t \leq 30\,\text{ms}$. The observer dynamics are affected by $M(\boldsymbol{q})$ resulting in a configuration depending and, thus, more difficult tuning of the observer dynamics. The plot depicts the results for initial conditions $\boldsymbol{q}_{01} = (0,\ 0,\ 0,\ 0,\ 0,\ 0,\ 0)$ rad and $\boldsymbol{q}_{02} = (0,\ 1.3,\ 0,\ 1.3,\ 0,\ 1,\ 0)$ rad. The current configuration significantly influences the observer dynamics. Moreover, although $M^{-1}(\boldsymbol{q})$ is bounded, some of its components may reach rather high values, thus acting as observer gains, possibly causing numerical problems. However, for the subsequent experiments the results are satisfactory and led to good performance.

With the observed joint accelerations $\hat{\ddot{\boldsymbol{q}}}$, one may now easily obtain the Cartesian accelerations and, consequently, also the

according signal flow diagram. Note that the estimated external torque $\hat{\boldsymbol{\tau}}_{\text{ext}}$ [see (83)], is already shown as a compensator for the unknown disturbance $\boldsymbol{\tau}_{\text{ext}}$. This compensation is not yet considered in the subsequent analysis of the observer dynamics and stability. Its benefit for the acceleration estimation is shown in Fig. 23.

The observer error $\boldsymbol{e}$ and its dynamics are given by

$$\boldsymbol{e} : = \hat{\dot{\boldsymbol{q}}} - \dot{\boldsymbol{q}} \tag{67}$$

$$\dot{\boldsymbol{e}} = \hat{M}^{-1}(\boldsymbol{q})(\boldsymbol{\tau} - \hat{\boldsymbol{n}}(\boldsymbol{q}, \dot{\boldsymbol{q}}) - K_O(\hat{\dot{\boldsymbol{q}}} - \dot{\boldsymbol{q}}))$$
$$- M^{-1}(\boldsymbol{q})(\boldsymbol{\tau} - \boldsymbol{n}(\boldsymbol{q}, \dot{\boldsymbol{q}}) + \boldsymbol{\tau}_{\text{ext}}). \tag{68}$$

Under ideal conditions [$\hat{M}(\boldsymbol{q}) = M(\boldsymbol{q})$, $\hat{\boldsymbol{n}}(\boldsymbol{q}, \dot{\boldsymbol{q}}) = \boldsymbol{n}(\boldsymbol{q}, \dot{\boldsymbol{q}})$], the error dynamics become

$$\dot{\boldsymbol{e}} = -M^{-1}(\boldsymbol{q}) K_O \boldsymbol{e} - M^{-1}(\boldsymbol{q}) \boldsymbol{\tau}_{\text{ext}} \tag{69}$$

$$K_O^{-1} M(\boldsymbol{q}) \dot{\boldsymbol{e}} + \boldsymbol{e} = -K_O^{-1} \boldsymbol{\tau}_{\text{ext}} \tag{70}$$

where $-M^{-1}(\boldsymbol{q}) K_O$ is the time-varying system matrix. Since the inertia matrix $M(\boldsymbol{q})$ has an upper and lower bound for revolute joints only, e.g., [34], its inverse $-M^{-1}(\boldsymbol{q})$ and, therefore, also $-M^{-1}(\boldsymbol{q}) K_O$ are bounded. From the static disturbance gain matrix K_O^{-1} one can conclude that the influence of $\boldsymbol{\tau}_{\text{ext}}$ can be reduced with increasing observer gain.

wrenches due to load accelerations via the well-known relation

$$\hat{\ddot{\boldsymbol{x}}} = \dot{J}\hat{\dot{\boldsymbol{q}}} + J\hat{\ddot{\boldsymbol{q}}}. \tag{76}$$

In order to reconstruct the contact wrench due to ball contact, a wrist force/torque sensor can be used. However, this sensor does not only measure the contact wrench but also inertial and gravity effects of the robot parts attached to the force sensor, including the end-effector. Consequently, the sensor measures the wrench

$${}^{S}\boldsymbol{\mathcal{F}}_{\mathrm{meas}} = {}^{S}\boldsymbol{\mathcal{F}}_{\mathrm{ext}} + {}^{S}\boldsymbol{\mathcal{F}}_{\mathrm{load}} + {}^{S}\boldsymbol{\mathcal{F}}_{g} \tag{77}$$

$$= {}^{S}R_{EE}\,{}^{EE}\boldsymbol{\mathcal{F}}_{\mathrm{ext}} + \underbrace{{}^{S}\boldsymbol{\mathcal{F}}_{\mathrm{load}} + {}^{S}\boldsymbol{\mathcal{F}}_{g}}_{{}^{S}\boldsymbol{\mathcal{F}}_{\mathrm{load},g}} \tag{78}$$

which is expressed in the sensor frame $\{S\}$. The rotation ${}^{S}R_{EE} \in \mathbb{R}^{6\times 6}$ transforms a wrench expressed in $\{EE\}$ frame into the $\{S\}$ frame. For the desired estimation of ${}^{EE}\boldsymbol{\mathcal{F}}_{\mathrm{ext}}$, the load and gravitational effects obtaining ${}^{S}\boldsymbol{\mathcal{F}}_{\mathrm{load},g}$ have to be compensated, leading to the estimation

$${}^{EE}\hat{\boldsymbol{\mathcal{F}}}_{\mathrm{ext}} = {}^{EE}R_{S}\left({}^{S}\boldsymbol{\mathcal{F}}_{\mathrm{meas}} - {}^{S}\hat{\boldsymbol{\mathcal{F}}}_{\mathrm{load},g}\right) \tag{79}$$

of the contact wrench with

$${}^{S}\hat{\boldsymbol{\mathcal{F}}}_{\mathrm{load},g} = {}^{S}\hat{\boldsymbol{\mathcal{F}}}_{\mathrm{load}}(\hat{\ddot{\boldsymbol{x}}}) + {}^{S}\hat{\boldsymbol{\mathcal{F}}}_{g}(\boldsymbol{q}) \tag{80}$$

$$= I_{EE}^{*}\hat{\ddot{\boldsymbol{x}}} + \begin{pmatrix} m_{EE}^{*}\,{}^{S}R_{0}(\boldsymbol{q})\,{}^{0}\boldsymbol{g} \\ \boldsymbol{x}_{S,EE} \times m_{EE}^{*}\,{}^{S}R_{0}(\boldsymbol{q})\,{}^{0}\boldsymbol{g} \end{pmatrix}. \tag{81}$$

In (81), I_{EE}^{*} and m_{EE}^{*} denote the inertia and mass effectively acting at the force/torque sensor. These are slightly different compared to the inertia I_{EE} and mass m_{EE} of the end-effector since parts of the sensor and its housing are also included in I_{EE}^{*} and m_{EE}^{*}. The gravity vector ${}^{0}\boldsymbol{g}$ expressed in the base frame $\{0\}$ is transformed into the sensor frame by the matrix ${}^{S}R_{0}(\boldsymbol{q})$. The constant translation vector from the sensor to the end-effector is denoted by $\boldsymbol{x}_{S,EE}$ and is expressed in the sensor frame. The lower dashed box in Fig. 21 shows the resulting block diagram of the external force estimation.

In addition to the contact wrench ${}^{EE}\boldsymbol{\mathcal{F}}_{\mathrm{ext}}$ itself, its impact on the robot in form of the disturbance $\boldsymbol{\tau}_{\mathrm{ext}}$ can now be estimated and compensated in the acceleration observer in order to improve its accuracy. The torque $\boldsymbol{\tau}_{\mathrm{ext}}$ is generally caused by contacts at the end-effector $\boldsymbol{\tau}_{\mathrm{ext},EE}$ and along the links of the robot $\boldsymbol{\tau}_{\mathrm{ext,link}}$, i.e.,

$$\boldsymbol{\tau}_{\mathrm{ext}} = \boldsymbol{\tau}_{\mathrm{ext,link}} + \boldsymbol{\tau}_{\mathrm{ext},EE}. \tag{82}$$

Unintended collisions with the robot along its structure are not considered, i.e., $\boldsymbol{\tau}_{\mathrm{ext,link}} = \boldsymbol{0}$ and finally

$$\hat{\boldsymbol{\tau}}_{\mathrm{ext}} = J^{T}\,{}^{EE}\hat{\boldsymbol{\mathcal{F}}}_{\mathrm{ext}}. \tag{83}$$

Note that model uncertainties related to the end-effector are also included in the estimated external torque $\boldsymbol{\tau}_{\mathrm{ext}}$. The estimation of $\boldsymbol{\tau}_{\mathrm{ext}}$ is based on measurements but also on ${}^{S}\hat{\boldsymbol{\mathcal{F}}}_{\mathrm{load},g}$, which in turn depends on the observer outputs $\hat{\ddot{\boldsymbol{q}}}$ and $\hat{\dot{\boldsymbol{q}}}$. Therefore, feeding $\hat{\boldsymbol{\tau}}_{\mathrm{ext}}$ back into the observer for compensation changes the dynamics of the observer and the stability proof shown above for the observer without compensation does not hold any longer.
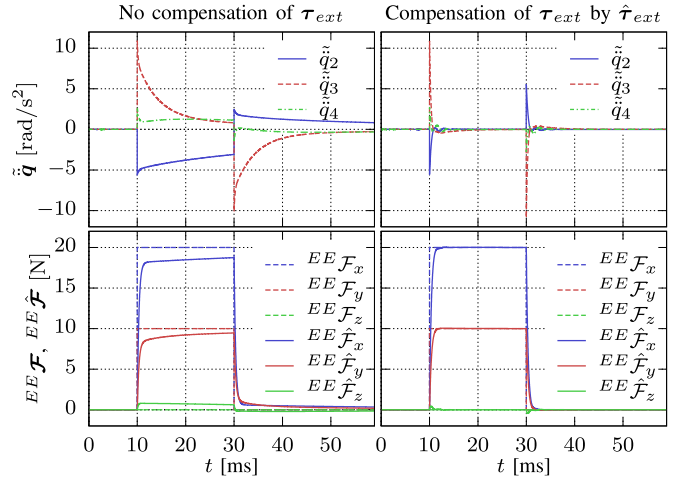
Fig. 23.   Observer error for the acceleration in axes 2, 3, and 4 (top left and right) and estimation of external forces (bottom left and right) for ${}^{EE}\boldsymbol{\mathcal{F}}_{\mathrm{ext}} = (20, 10, 0, 0, 0, 0)^{T}$ N for $10 \le t \le 30$ ms, $k_{O,i} = 50$ and $\boldsymbol{q}_{0} = (0, 1.3, 0, 1.3, 0, 1, 0)^{T}$ rad.

However, assuming a sufficient accurate model, the resulting precise estimation of ${}^{S}\hat{\boldsymbol{\mathcal{F}}}_{\mathrm{load},g}$ is compensated by ${}^{S}\boldsymbol{\mathcal{F}}_{\mathrm{load},g}$ in (79), which is the related part in the measured quantity. The impact of the additional observer feedback via $\hat{\boldsymbol{\tau}}_{\mathrm{ext}}$ might, therefore, be neglected compared to the nominal feedback K_{O}. This is confirmed by experimental results and simulations, where the observer with $\hat{\boldsymbol{\tau}}_{\mathrm{ext}}$ compensation remains stable.

The performance of the wrench estimation together with the compensation of external torques was verified by means of simulation. Fig. 23 depicts simulation results for an external wrench of ${}^{EE}\boldsymbol{\mathcal{F}}_{\mathrm{ext}} = (20, 10, 0, 0, 0, 0)^{T}$ N for $10 \le t \le 30$ ms. The effect of the resulting unknown external torques can be seen in the estimation errors for the acceleration and the external wrench (left subfigures). However, compensating the external torque by its estimation $\hat{\boldsymbol{\tau}}_{\mathrm{ext}}$ considerably improves the estimation results (right subfigures). The force/torque sensor at the end-effector is modeled by a first-order delay with a bandwidth of 500 Hz.

In summary, the observer presented in this section allows to estimate the external contact wrench ${}^{EE}\boldsymbol{\mathcal{F}}_{\mathrm{ext}}$ from the ball, which is required for the 6-Dof reference control described in Section IV-E.

E. 6-Dof Reference Control

In general, we intend to stabilize the ball at a steady point $\boldsymbol{x}_{B C_{\mathrm{des}}}$ (in fact at a projection on the horizontal plane). For the vertical motion, we refer to the scheme from Section III-C

$$z(t) = \begin{cases} A \sin\left(\dfrac{5\pi}{4T}t\right) + z_{0}, & \text{for } t \in \left[0; \dfrac{4}{5}T\right] \\[2mm] -\dfrac{1}{4}A \sin\left(\dfrac{5\pi}{T}t\right) + z_{0}, & \text{for } t \in \left]\dfrac{4}{5}T; T\right[. \end{cases} \tag{84}$$

Now, we incorporate also the horizontal ball motion. For stabilizing the lateral motion the hand needs to follow the observed ball position from Section IV-D. Since we want to control the ball in cylindrical coordinates (see Fig. 4), the resulting desired
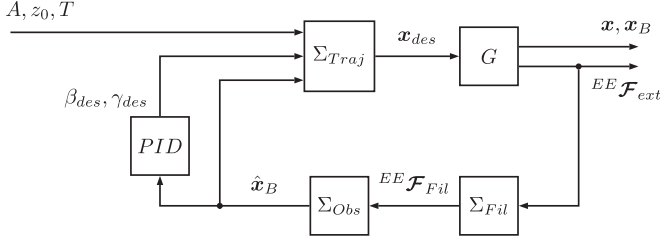
Fig. 24. Overall dribbling controller consists of the trajectory generator, the ball observer and the wrench filter. The trajectory generator takes into account the ball estimation coming from the ball observer, which is purely generated from interaction force measurement.

position of the robot hand following the ball is

$$\begin{bmatrix} x_{\text{des}} \\ y_{\text{des}} \\ \varphi_{\text{des}} \end{bmatrix} = \begin{bmatrix} -(d_B - \Delta_H)\sin(\varphi_B) \\ (d_B - \Delta_H)\cos(\varphi_B) \\ \varphi_B \end{bmatrix} \quad (85)$$

with Δ_H being an offset from the $\{EE\}$ coordinate system to the middle of the finger. For attracting the ball to its desired horizontal position $\boldsymbol{x}_{B_{C_{\text{des}}}}$, we use a simple PID control for the two remaining hand rotations β and γ

$$\beta_{\text{des}} = K_{P\beta}(d_{B_{\text{des}}} - d_B) + K_{D\gamma}(\dot{\varphi}_{B_{\text{des}}} - \dot{\varphi}_B)$$
$$+ K_{I\beta} \int_0^t (d_{B_{\text{des}}} - d_B)\mathrm{d}\tau \quad (86)$$

$$\gamma_{\text{des}} = K_{P\gamma}(\varphi_{B_{\text{des}}} - \varphi_B) + K_{D\gamma}(\dot{\varphi}_{B_{\text{des}}} - \dot{\varphi}_B)$$
$$+ K_{I\gamma} \int_0^t (\varphi_{B_{\text{des}}} - \varphi_B)\mathrm{d}\tau \quad (87)$$

with $K_{\{PID\},\{\beta\gamma\}}$ being the respective gains for the PID control.

The overall structure of the closed-loop system is shown in Fig. 24. A, z_0, and T are specified by the user for the given parameters of the z-axis trajectory. G denotes the robot ball model. Its measured outputs are the contact force wrench $^{EE}\boldsymbol{\mathcal{F}}_{\text{ext}}$ and the robot position $\boldsymbol{x}$. $^{EE}\boldsymbol{\mathcal{F}}_{\text{ext}}$ is filtered in Σ_{Fil}. This filtered signal $^{EE}\boldsymbol{\mathcal{F}}_{\text{Fil}}$ is fed to the observer Σ_{Obs} in order to construct the position estimate $\hat{\boldsymbol{x}}_B$, which is then used in the control laws given by (86) and (87).

In order to prepare future experiments with intrinsically elastic systems such as the DLR hand-arm system, we decided to interface the LWR-III from the trajectory generation side via Cartesian impedance control. This can be considered as the closest approximation of a full passively compliant system that can be realized with the LWR-III. Therefore, we shortly summarize the main characteristics of the used scheme.

F. Cartesian Impedance Controller

Based on the elastic joint model described in Section II-B4 following controller structure[8] is used for controlling the full robot dynamics simulation and the real robot. It enables high-performance Cartesian impedance control at a rate of 1 kHz with

velocity feedforward. The closed-form solution of the overall scheme can be written as

$$\boldsymbol{u} = -J(\bar{\boldsymbol{q}})^T(K_x\tilde{\boldsymbol{x}}(\bar{\boldsymbol{q}}) + D_x\dot{\tilde{\boldsymbol{x}}}(\bar{\boldsymbol{q}})) + \bar{\boldsymbol{g}}(\boldsymbol{\theta}) \quad (88)$$

where $\boldsymbol{u}$ is a new control input (instead of motor torque) for a lower level full state feedback controller that is however omitted for brevity (incorporation of motor position, joint torque, and their respective derivatives) [36]. The impedance controller is designed with $K_x, D_x \in \mathbb{R}^{m \times m}$, which are the diagonal positive definite desired stiffness and damping matrices. $\boldsymbol{x}_d \in \mathbb{R}^m$ is the desired tip position in Cartesian coordinates, which is commanded via the control law described in the previous subsection and $\tilde{\boldsymbol{x}}(\bar{\boldsymbol{q}}) = \boldsymbol{x}(\bar{\boldsymbol{q}}) - \boldsymbol{x}_d$. $\boldsymbol{x}(\bar{\boldsymbol{q}}) = T(\bar{\boldsymbol{q}})$ is the forward kinematics map. $\bar{\boldsymbol{q}} = h^{-1}(\boldsymbol{\theta})$ is the static equivalent of $\boldsymbol{q}$. The gravity compensation term $\bar{\boldsymbol{g}}(\boldsymbol{\theta})$ is a function of the motor position and is designed in such a way, that it provides exact gravity compensation in static case. In the simulation and experiments, we selected K_x to be $K_x = \text{diag}\{1500\ 1500\ 1500\ 200\ 200\ 200\}$ (translational stiffness in N/m and rotational stiffness in Nm/rad).

Note that the effective stiffness resulting from the hand together with the robot arm might be dynamically adapted in order to move the stiffness depending stability areas (see Figs. 15 and 16) over the desired operating point. When, e.g., reducing the amplitude A and the cycle time T during dribbling, it is advisable to increase the stiffness in order to keep the operating point (A, T) within the stability areas or even within the inscribed circles.

V. SIMULATIONS AND EXPERIMENTS

In this section, we show simulation results for the proposed model and observer, as well as provide a human dribbling analysis. Before going into the details of our robot dribbling simulations and experimental results, we analyze dribbling measurements obtained via passive marker tracking of a semipro human basketball player. Our theoretical dribbling model is used to analyze this human manipulation skills. The resulting dribbling parameters of our presented methods are fitted to the real dribbling motions showing good consistency. Subsequently, a stability analysis of the real human motions is presented.

A. Human Dribbling Measurement

For capturing human dribbling, the position and velocity were obtained with a Vicon passive marker tracking system. The system consists of eight cameras running at 180 Hz and several markers on the human arm and ball ensured the observability over the full cycle. Overall, it can be seen that the curves from Section IV-C and the human measurement look qualitatively the same.[9]

Fig. 25 (left and center) depicts the locations of the tracked markers that were attached to the arm, hand, and ball. The markers of the ball were placed such that both, its position and orientation could be extracted despite occlusion during hand contact. Fig. 25 (right) depicts a visualization of a tracked pose

---

[8]Please note that this is a simplified view on the structure, which was chosen for better understanding.

[9]Please note that the offset is not subtracted, as for human measurement it is not exactly known.

Fig. 25. Setup and marker positions for the human dribbling experiments (left and center), sample data of a tracked pose visualized in ViconIQ (right).
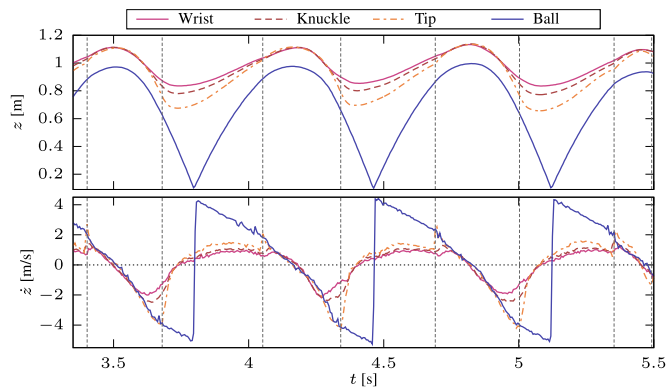

Fig. 26. Dribbling position and velocity of a semipro human player, begin and end of contact phases are indicated by vertical dashed lines.
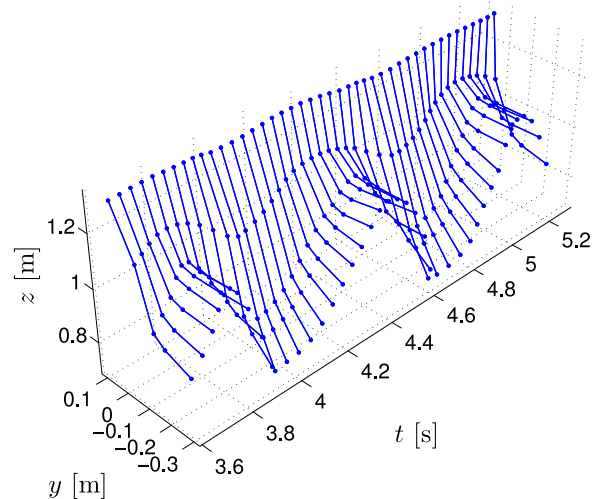

Fig. 27. Tracked arm/hand configuration for human dribbling of a semipro human player.

TABLE II
OPTIMAL PARAMETERS OF THE HAND TRAJECTORY (23) AND BALL DYNAMICS (2)

Fitted param.	K_H	z_0	A	t_0	p	$E\{e^2\}$
K_H, z_0,	**42**	**0.707**	0.287	0.000	0.800	7.0e−04
K_H, z_0, t_0, p	**77**	**0.790**	0.267	**0.123**	**0.601**	2.8e−04
Lower bound	0	0.200	—	−0.600	0.050	
Upper bound	1000	1.600	—	0.600	0.950	

including the human hand and the ball. In Fig. 26 some sample cycles of the measured position (upper) and velocity (lower) for the ball and three hand markers are shown. Interesting to notice is that besides the vertical motion the hand also performs a rotation around the radial axes of the hand which can be observed from the velocity plot (Fig. 26, lower), where the wrist and knuckle of the middle finger stop accelerating at the end of the hand contact. Then, the fingertip guides the ball and injects the most significant amount of energy into it.

The above mentioned wrist rotation is also visible in Fig. 27, where the arm motion is shown along the time axis. The indicated points from top to bottom are the shoulder, elbow, wrist, knuckle of the middle finger, and tip of the middle finger. It is clear that the two lowest lines, which represent the palm and the finger, are rotating.

B. Human Dribbling Analysis

The captured data is used to analyze the human dribbling with the framework presented in this paper. Directly using the measured human hand motion for fitting the model parameters K_H and z_0 of the hand trajectory (23) would lead to a similar hand trajectory but not necessarily to a suitable dribbling cycle of the ball. Instead, the model parameters were optimized based on the dynamical model (2) of the ball from hand contact until next ground contact for minimizing the integrated squared er-

ror between simulated and measured ball motion. This ensures best possible ball motions given a certain trajectory form. As depicted in Fig. 11(a), the hand trajectory $z(t)$ starts at each ground contact of the ball, where the time is reset to $t = 0$. The amplitude A of the hand trajectory is not independently tunable, since it is derived from z_0 in order to guarantee that the hand gets contact to the ball at the beginning of the model contact sequence. The time T for the mean of a complete cycle is defined by the experiment itself and was therefore not fitted either.

The fitting was carried out with the following two different approaches.
1) The time shifting and relation of the sine half-waves was kept fixed to $t_0 = 0$ and $p = 4/5$.
2) The time shifting and the relation of the sine half-waves are subject to the fitting procedure, i.e., $p \neq 4/5$ and $t_0 \neq 0$.

The model parameters were fitted by minimizing the squared error sum between $\hat{z}_{1B}$ and z_{1B} using Octave's sqp function with the default tolerance 1.5e−8 and the constraints, as shown in Table II. The optimal parameters and the related mean squared error $E\{e^2\}$ (per datapoint) are listed in Table II.

Fig. 28 depicts results from the first fitting approach (first row in Table II). It shows the simulated ($\hat{z}_{1B}$) and measured (z_{1B}) ball position during the fitted contact and postcontact interval
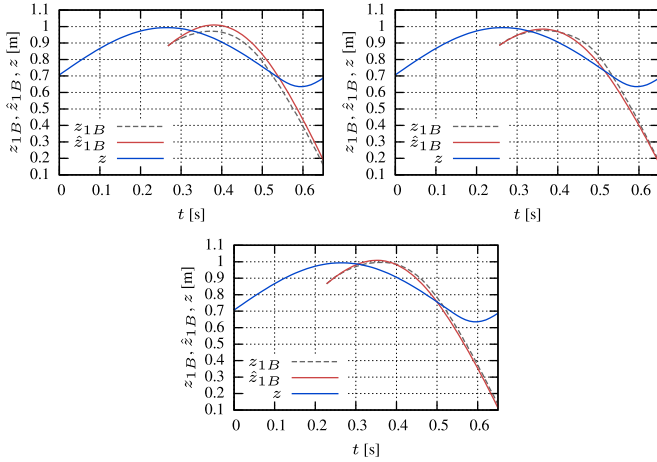
Fig. 28.   Measured ball position z_{1B} during the three phases from hand contact until next ground contact (Fig. 26) and simulated ball position $\hat{z}_{1B}$ where the parameters K_H and z_0 are fitted over all shown phases via minimizing the squared error between ball dynamics (2) together with hand trajectory (23) and measurements.
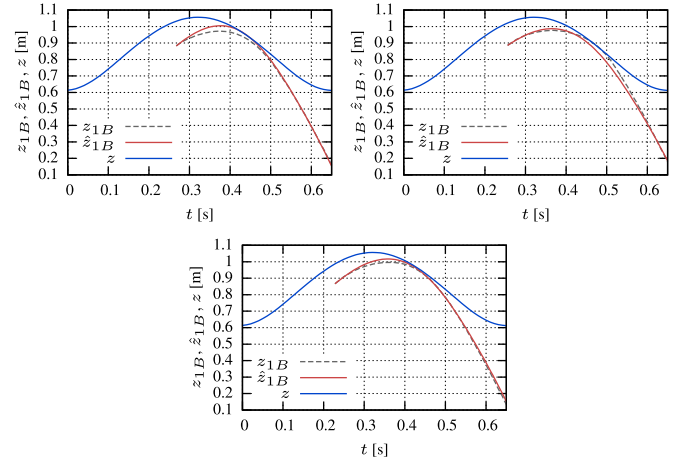
Fig. 29.   Measured ball position z_{1B} during the three phases from hand contact until next ground contact (see Fig. 26) and simulated ball position $\hat{z}_{1B}$ where the parameters K_H and z_0 together with the time shift t_0 and the relation p are fitted in order to minimize the squared error between ball dynamics (2) together with hand trajectory (23) and measurements.

as well as the resulting hand trajectory over the full measured cycle for each of the three analyzed phases.

The ball trajectory is fitted rather well, especially immediately before the next ground contact, which is important for a correct ball trajectory in the upwards phase before the next hand contact. The observed human dribbling can, thus, be modeled very well with the hand trajectory (23) together with a stiffness $K_H = 42$ N/m. However, K_H is estimated much lower than the expected value of $K_H > 200$ N/m. A possible explanation of this effect is, that a human declines the wrist at the beginning of the hand contact leading to a smaller stiffness. As shown in Section I, Table I, a small stiffness around $K_H \approx 50 \ldots 100$ N/m results in a small required maximal power $P_{\max}$ and force $F_{\max}$. From this, a possible explanation might be that a human adapts the resulting hand stiffness toward lower values by declining the wrist in order to reduce maximal power and force.

Comparing the measured hand trajectories in Fig. 26 with the hand trajectory (23) leads to the conclusion that a fixed relation $p = 4/5$ between the slow and fast sine half-wave without time shift t_0 might be a too restrictive assumption. Letting also p and t_0 free leads to even better results, see Fig. 29 and the second row of Table II. On the one hand, the error between measured and simulated ball trajectories is smaller. On the other hand, the parameter optimization leads to a more realistic stiffness $K_H = 77$ N/m.

The resulting areas of stable dribbling cycles (ref. Section III) for the optimized parameter sets in both approaches are shown in Fig. 30. With $p = \frac{4}{5}$ and $t_0 = 0$ the resulting combination of T and A lies within the stable area but rather close to its upper bound. When also fitting the parameters p and t_0 of the hand trajectory, the resulting parameter combination for T and A provides a significantly larger stability margin.

The hand trajectory $z(t)$ with optimized parameters z_0, t_0, and p is compared to the real human hand movement, see Fig. 31. The proposed model reasonably explains the measured finger tip trajectory. Differences may have multiple causes. For example,
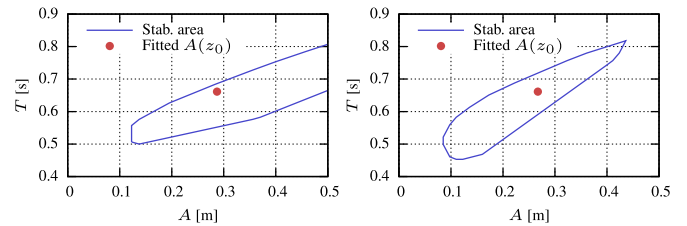

Fig. 30.   Operating point and stability regions for the two approaches. Left: only K_H and z_0 are optimized with fixed relation p of the two sine half-waves and time shift t_0 right: p and t_0 are also optimized.
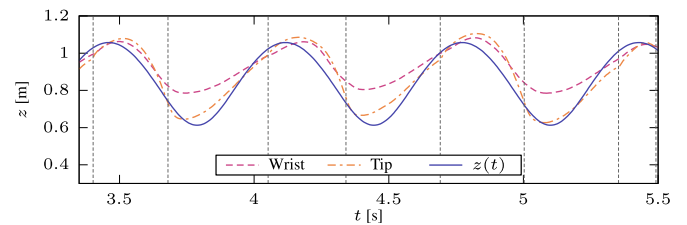

Fig. 31.   Measured human hand position (wrist and tips, marker offset corrected) compared to hand trajectory with optimized parameters (t_0, p also fitted), begin and end of contact phases are indicated by vertical dashed lines.

the human hand pitching for achieving the required amplitude is not yet considered. Still, note that the ball motions that result from these different hand movements are almost identical.

In summary, the following can be concluded from the analyses above.

1) Our modeling framework also allows us to model human dribbling cycles with rather high accuracy.
2) The hand stiffness K_H is found to be lower than expected by our rather simple model. We conclude that the effective stiffness in humans is reduced by declining the wrist at the beginning of the hand-ball contact for reducing peak power and force.
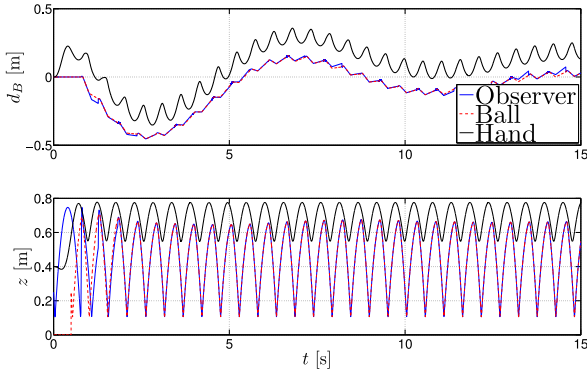
Fig. 32. Position for a simulation with a 3-DoF ball. The upper plot shows the distal coordinate, while the lower one depicts the actual dribbling motion.

3) A fixed relation $p = 4/5$ of the two sine half-waves of the hand trajectory without time shift t_0 is too restrictive for explaining human dribbling. Optimizing these two parameters further improves the fitting results and leads to a larger stability margin of the dribbling cycles.

4) The framework might be used in future research works for evaluating and optimizing human dribbling with respect to stability as well as required peak force and power.

Next, we analyze the multi-DoF robot dribbling cases. The simulation results shown in Section V-C are planar, i.e., the ball has 3 DoF. The robot is modeled as a velocity source on which the elastic finger is mounted. Basically, we lock the adaptation of the translation in x-direction and the rotations about the y- and z-axis in the model from Section II.

C. Simulation With a 3 DoF Ball in $2-D$ Space

For this first simulation, we assume the robot to be a position/velocity source (i.e., ideal dynamic trajectory tracking). In all simulations and experiments, we use following material parameters of the robot hand (see Fig. 5) for calculating the reflected contact stiffness: $E = 210000$ N/mm^2, $I_y = bh^3/12$, $b = 30$ mm, and $h = 1$ mm. Fig. 32 depicts the resulting ball, observer, and hand motion. In the upper plot the lateral position is shown. The steady-state point of the ball is located at $d_B = 0$. The hand is expressed in $\{EE\}$, which leads to the shift of the hand with respect to the ball (finger length). Clearly, the ball stabilizes at the desired position. In the lower plot, the vertical position is depicted. In this direction, we obtain a stable cycle for the ball motion. Furthermore, we see that the observer converges within two cycles toward the true ball trajectory.

D. Simulation With a 6-DoF Ball in $3-D$ Space

The simulation results presented now are done with the full dynamic model of the LWR-III (see Section II-B4) that is controlled via Cartesian impedance control (see Section IV-F).

Fig. 33 again depicts the ball and hand position expressed in $\{W\}$ for a regulation dribbling task, however, this time for a full simulation of robot and impedance controller. Please note that the same y-axis offset as for the 3-DoF simulation is present. As
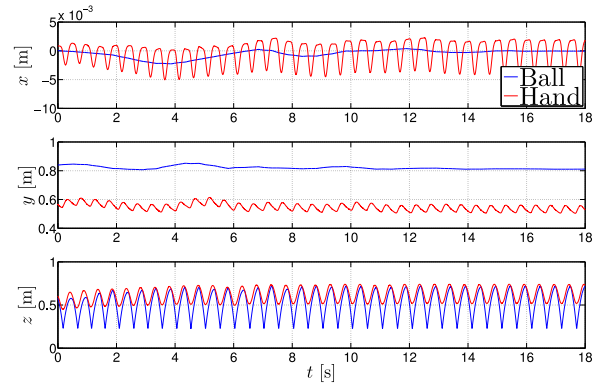

Fig. 33. Relevant ball coordinates for a full dynamic simulation (robot modeled as a flexible joint robot, full-state feedback controller for the motor and overlaid Cartesian impedance controller) with a 6-DoF ball.
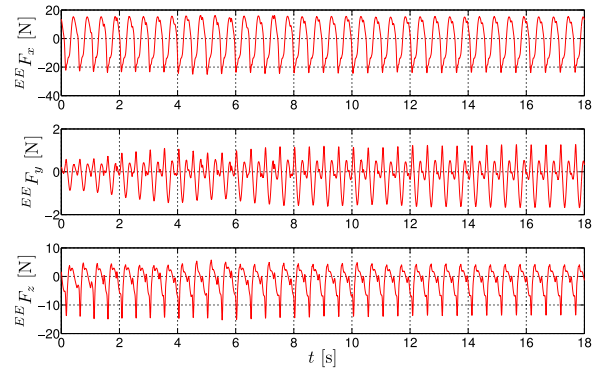

Fig. 34. Contact forces for a full dynamic simulation (robot modeled as a flexible joint robot, full-state feedback controller for the motor, and overlaid Cartesian impedance controller) with a 6-DoF ball.
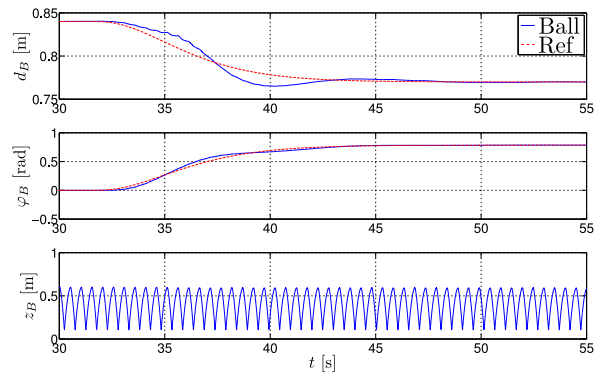

Fig. 35. Relevant ball coordinates for a tracking dribbling simulation (online setpoint adjustment) with a 6-DoF ball.

one can see the motion converges quickly to the desired stable dribbling cycle in all three axes. Fig. 34 shows the contact forces expressed in $\{EE\}$. The maximal contact force is ≈ 20 N along the x-axis. The forces in the z-axis are caused by the friction of the ball.

Fig. 35 shows that it is also possible to vary the lateral setpoint and desired distal point online, i.e., with the designed controller the robot is able to follow a desired dribbling trajec-
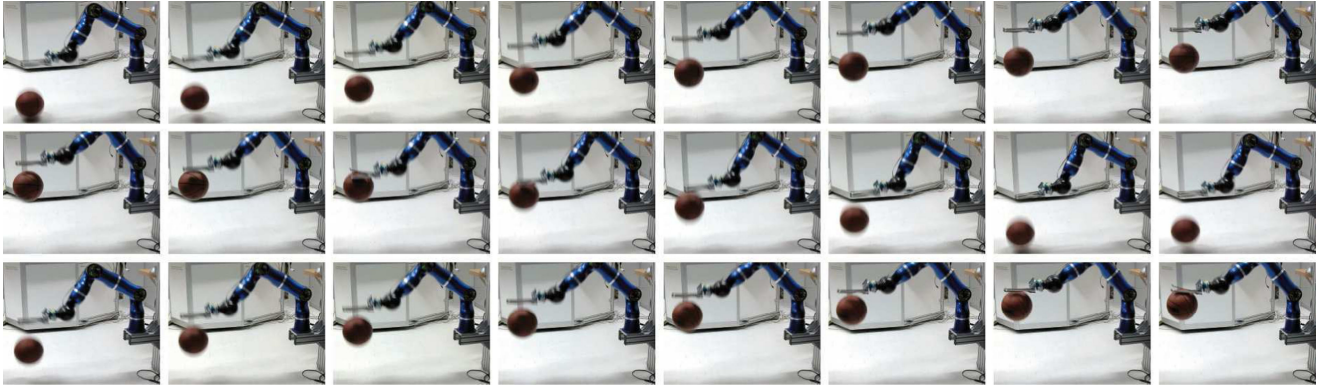
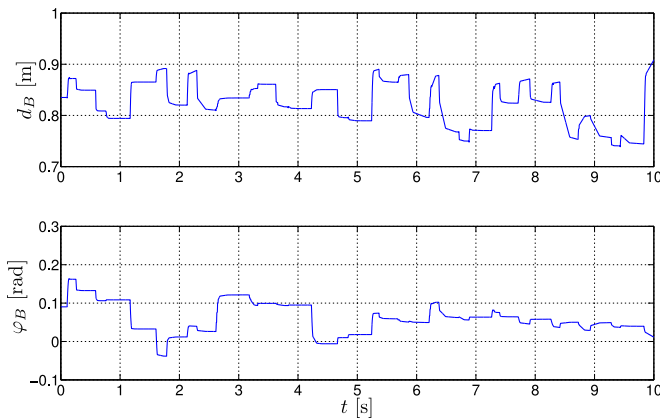Fig. 36.   Snapshots from basketball dribbling with the LWR-III that is equipped with an elastic hand.

Fig. 37.   Distal coordinate d_B and rotation φ_B measured for a the LWR-III dribbling experiment.
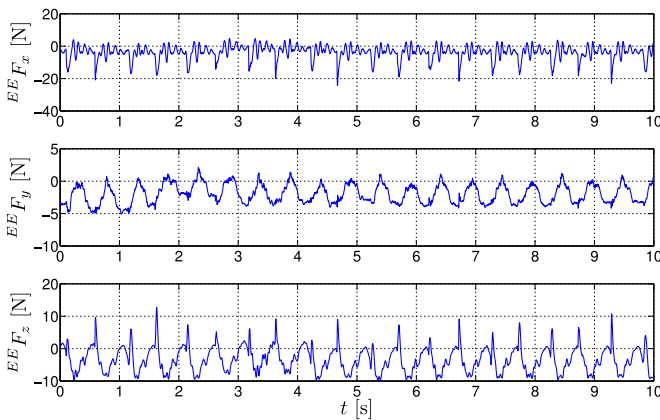

Fig. 38.   Force $^{EE}\boldsymbol{F}$ at the end-effector during the experiment.

tory $[d_B(t), \varphi_B(t)]$ without destabilization. The possible online adjustment of dribbling frequency, dribbling height, and amplitude is not shown for brevity. However, this can be viewed in the video. In the depicted simulation, the robot performs a simultaneous rotation of 45º and distal motion of 7 cm. Clearly, the dribbling cycle is maintained.

The experimental validation with the LWR-III that is equipped with an elastic hand is described next.

E. 6-DoF Experiments With LWR-III

Fig. 36 shows an image series of successful elastic dribbling with a LWR-III. The utilization of the elastic fingers can be clearly observed. A sample measurement is depicted in Figs. 37 and 38. In Fig. 37, the ball position in cylindrical coordinates d_B and φ_B is shown. In Fig. 38, we find the disturbance compensated end-effector forces. The maximal force in the upper plot is in a similar range as for the 6-DoF simulation, see Fig. 34. Furthermore, the finger oscillations can be observed mainly in x-direction of $\{EE\}$. Overall, the robot is able to stabilize the motion of the ball.

VI. CONCLUSION

In this paper, we developed a theoretical foundation for blind dribbling with an intrinsically elastic robot. We show the stability of a limit cycle with a perturbation approach and the cycle stability for a finite-time convergence sliding mode observer. This scheme is suitable to observe the ball motion even for the partially observable cycle with force sensing only, i.e., no vision information is necessary for our approach, though it could be easily integrated. Based on this conceptual design, we derived significant beneficial effects of intrinsic elasticity in terms of required peak power, impact force, and robustness compared to stiff actuation.

In order to support the theoretical contribution, we extend the results to stable dribbling with an intrinsically compliant robot. Based on force sensing together with an acceleration observer and associated "haptic" ball observation only, we were able to reactively adjust the robot motion such that system errors (ball, robot, and sensing uncertainties) can be coped with. The robustness of the proposed method, which incorporates intrinsic contact compliance and resulting energy transfers, shows the large benefit one can gain from intrinsically compliant actuation in terms of cycle stability, robustness, and manipulability.

Finally, the proposed framework was applied to captured data from human dribbling. As a result, the dribbling cycles of humans could be accurately described and analyzed by our proposed models.

ACKNOWLEDGMENT

REFERENCES

[1] A. Albu-Schäffer, S. Haddadin, C. Ott, A. Stemmer, T. Wimböck, and G. Hirzinger, "The DLR lightweight robot—Lightweight design and soft robotics control concepts for robots in human environments," *Ind. Robot J.*, vol. 34, no. 5, pp. 376–385, 2007.

[2] Rethink Robotics, *Smart, Collaborative Robot for Precision Tasks*, sawyer Datasheet, Accessed on: Oct. 6, 2017. [Online]. Available: http://www.rethinkrobotics.com/wp-content/uploads/2015/11/Sawyer_Datasheet_Nov_2015_web.pdf

[3] Franka Emika, Panda. Accessed 2017-10-06. [Online]. Available: https://www.franka.de/

[4] S. Haddadin, M. Weis, S. Wolf, and A. Albu-Schäffer, "Optimal control for maximizing link velocity of robotic variable stiffness joints," in *Proc. IFAC World Congr.*, Milano, Italy, 2011, pp. 6863–6871.

[5] M. Stilman, D. Baglino, and A. Lillie, "Robot dribbling a ball," 2001, Accessed on: Oct. 6, 2017. [Online]. Available: http://www.flyingpudding.com/projects/robot_dribble/

[6] D. Shiokata, A. Namiki, and M. Ishikawa, "Robot dribbling using a high-speed multifingered hand and a high-speed multifingered hand and a high-speed vision system," in *Proc. IEEE/RSJ Int. Conf. Intell. Robots Syst.*, Edmonton, Canada, 2005, pp. 3945–3950.

[7] G. Bätz, M. Sobotka, D. Wolherr, and M. Buss, "Robot basketball: Ball dribbling—A modified juggling task," in *Proc. IEEE Int. Conf. Robot. Autom.*, San Diego, CA, USA, 2008, pp. 2410–2415.

[8] G. Bätz, K. K. Lee, D. Wollherr, and M. Buss, "Robot basketball: A comparison of ball dribbling with visual and force/torque feedback," in *Proc. IEEE Int. Conf. Robot. Autom.*, Kobe, Japan, 2009, pp. 514–519.

[9] U. Mettin, A. S. Shiriaev, G. Bätz, and D. Wolherr, "Ball dribbling with an underactuated continuous-time control phase," in *Proc. IEEE Int. Conf. Robot. Autom.*, Anchorage, AK, USA, 2010, pp. 4669–4674.

[10] A. Pekarovskiy, K. Saluja, R. Sarkar, and M. Buss, "Resonance-driven dynamic manipulation: Dribbling and juggling with elastic beam," in *Proc. IEEE Int. Conf. Robot. Autom.*, 2014, pp. 943–948.

[11] M. Bühler, D. E. Koditschek, and P. Kindlmann, "A one degree of freedom juggler in a two degree of freedom environment," in *Proc. IEEE Int. Workshop Intell. Robots*, Tokyo, Japan, 1988, pp. 91–97.

[12] R. Ronsse, P. Lefevre, and R. Sepulchre, "Rhythmic feedback control of a blind planar juggler," *IEEE Trans. Robot.*, vol. 23, no. 4, pp. 790–802, Aug. 2007.

[13] P. Reist and R. D'Andrea, "Bouncing an unconstrained ball in three dimensions with a blind juggling robot," in *Proc. IEEE Int. Conf. Robot. Autom.*, Kobe, Japan, 2009, pp. 1774–1781.

[14] S. Haddadin, K. Krieger, and A. Albu-Schaffer, "Exploiting elastic energy storage for cyclic manipulation: Modeling, stability, and observations for dribbling," in *Proc. 50th IEEE Conf. Decision Control Eur. Control Conf.*, Orlando, FL, USA, 2011, pp. 690–697.

[15] S. Haddadin, K. Krieger, M. Kunze, and A. Albu-Schaffer, "Exploiting potential energy storage for cyclic manipulation: An analysis for elastic dribbling with an anthropomorphic robot," in *Proc. IEEE/RSJ Int. Conf. Intell. Robots Syst.*, San Francisco, CA, USA, 2011, pp. 1789–1796.

[16] J. Yamaguchi, D. Nishino, and A. Takanishi, "Realization of dynamic biped walking varying joint stiffness using antagonistic driven joints," in *Proc. IEEE Int. Conf. Robot. Autom.*, Leuven, Belgium, 1998, pp. 2022–2029.

[17] M. Okada, S. Ban, and Y. Nakamura, "Skill of compliance with controlled charging/discharging of kinetic energy," in *Proc. IEEE Int. Conf. Robot. Autom.*, Washington, DC, USA, 2002, pp. 2455–2460.

[18] J. J. Fontanella, *The Physics of Basketball*. Baltimore, MD, USA: The John Hopkins Univ. Press, 2006.

[19] R. C. Hibbeler, *Engineering Mechanics*. Englewood Cliffs, NJ, USA: Prentice-Hall, 2010.

[20] FIBA, "Official basketball rules 2014: Basketball equipment. Fédération Internationale de Basketball (FIBA)," Oct. 2014, Accessed on: Oct. 6, 2017. [Online]. Available: http://www.fiba.com/downloads/Rules/2014/BasketballEquipment2014_Final_V1_withCovers_LOW.pdf

[21] K. Waldron and J. Schmiedeler, *Springer Handbook of Robotics*, B. Siciliano and O. Khatib, Eds. New York, NY, USA: Springer, 2005.

[22] K. H. Hunt and F. R. E. Crossley, "Coefficient of restitution interpreted as damping in vibroimpact," *J. Appl. Mech.*, vol. 42, pp. 440–445, 1975.

[23] C. C. de Wit and P. Tsiotras, "Dynamic tire friction models for vehicle traction control," in *Proc. 38th IEEE Conf. Decision Control*, Phoenix, AZ, USA, 1999, pp. 3746–37 251.

[24] K. Gieck and R. Gieck, *Engineering Formulas*. Germering, Germany: Gieck, 1997.

[25] D. Gross, W. Hauger, J. Schröder, W. Wall, and J. Bonet, *Engineering Mechanics 2: Mechanics of Materials*. Heidelberg, Germany: Springer, 2011.

[26] M. Spong, "Modeling and control of elastic joint robots," *J. Dyn. Syst., Meas., Control*, vol. 109, no. 4, pp. 291–300, 1987.

[27] I. R. Manchester, "Transverse dynamics and regions of stability for nonlinear hybrid limit cycles," *IFAC Proc. Volumes*, vol. 44, no. 1, pp. 6285–6290, 2011. [Online]. Available: http://www.sciencedirect.com/science/article/pii/S1474667016446124

[28] I. R. Manchester, M. M. Tobenkin, M. Levashov, and R. Tedrake, "Regions of attraction for hybrid limit cycles of walking robots," *IFAC Proc. Volumes*, vol. 44, no. 1, pp. 5801–5806, 2011. [Online]. Available: http://www.sciencedirect.com/science/article/pii/S1474667016445325

[29] R. Goebel and A. R. Teel, "Preasymptotic stability and homogeneous approximations of hybrid dynamical systems," *SIAM Rev.*, vol. 52, no. 1, pp. 87–109, 2010. [Online]. Available: http://www.jstor.org/stable/25662361

[30] S. V. Drakunov, "Sliding-mode observer based on equivalent control method," in *Proc. 31st IEEE Conf. Decision Control*, Tucson, AZ, USA, 1992, pp. 2368–2369.

[31] K. H. Khalil, *Nonlinear Systems*. Englewood Cliffs, NJ, USA: Prentice-Hall, 2002.

[32] D. Gross, W. Hauger, and J. Schröder, *Engineering Mechanics 1: Statics*. Heidelberg, Germany: Springer, 2009.

[33] S. Haddadin, *Towards Safe Robots* (Springer Tracts in Advanced Robotics, vol. 90). Berlin, Germany: Springer, 2014.

[34] F. Ghorbel, B. Srinivasan, and M. W. Spong, "On the uniform boundedness of the inertia matrix of serial robot manipulators," *J. Robot. Syst.*, vol. 15, no. 1, pp. 17–28, 1998.

[35] A. van den Bos, *Appendix C: Positive Semidefinite and Positive Definite Matrices*. Hoboken, NJ, USA: Wiley, 2007, pp. 259–263.

[36] A. Albu-Schäffer, C. Ott, and G. Hirzinger, "A unified passivity-based control framework for position, torque and impedance control of flexible joint robots," *Int. J. Robot. Res.*, vol. 26, pp. 23–39, 2007.

Sami Haddadin (M'11) received the degrees in electrical engineering (Dipl.-Ing., 2005) and in computer science (M.Sc., 2009) from Technical University of Munich (TUM), Munich, Germany, in technology management (Honours Degree, 2007) from Ludwig Maximilian University and TUM, Munich, Germany, and the Ph.D. degree in safety in robotics from RWTH Aachen University, Aachen, Germany in 2011.

He is currently a Full Professor and the Director in the Institute of Automatic Control, Leibniz University Hannover, Hanover, Germany. He organized/edited several international robotics conferences and journals and published more than 140 scientific articles. His research interests include physical human-robot interaction, nonlinear robot control, real-time motion planning, real-time task and reflex planning, robot learning, optimal control, human motor control, variable impedance actuation, and safety in robotics.

Dr. Haddadin received numerous awards at the top international robotics conferences and journals. Among other things, he received the 2015 IEEE/RAS Early Career Award, the 2015 RSS Early Career Spotlight, the 2015 Alfred Krupp Award, the 2017 Deutscher Zukunftspreis (German President's Award for Innovation in Science and Technology), and was selected in 2015 and 2016 as Capital Young Elite Leader under 40 in Germany for the domain "Politics, State, & Society."

Kai Krieger recieved the Dipl.-Ing. degree in mechatronics from University of Stuttgart, Stuttgart, Germany, in 2011.

From 2010 to 2013, he has been with the Institute of Robotics and Mechatronics, German Aerospace Center, Cologne, Germany. In 2013, he joined Beckhoff Automation GmbH & Co. KG. His research interests include physical human robot interaction, nonlinear robot control, dynamic manipulation, and multibody dynamics.

Torsten Lilge received the Dipl.-Ing. degree in electrical engineering in 1991 and the Ph.D. degree in nonlinear observers in 1999, both from University of Hannover, Hanover, Germany.

He is currently a Senior Researcher and Lecturer in the Institute of Automatic Control, Leibniz University of Hanover, Hanover, Germany. He participated in research projects and activities related to nonlinear observers, data fusion, and nonlinear control. He has published more than 20 papers in journals, conferences, and books. His main research interests include the design of nonlinear observers, as well as their application to model based data fusion and disturbance reconstruction in different domains.

Alin Albu-Schäffer (F'16) received the Engineering degree in electrical engineering from the Technical University of Timisoara, Romania, in 1993 and the Ph.D. degree in control systems from the Technical University of Munich (TUM), Germany, in 2002.

Since 1995, he has been with Institute of Robotics and Mechatronics, German Aerospace Center (DLR), Cologne, Germany. In 2012, he became the Head of this Institute and a Full Professor at Technical University of Munich. His personal research interests include robot design, modeling and control, flexible joint and variable compliance robots for manipulation and locomotion, physical human-robot interaction, and bioinspired robot design.

Dr. Albu-Schäffer and his team received numerous awards, among them the IEEE King-Sun Fu Best Paper Award of the Transactions on Robotics in 2012 and 2014, several ICRA and IROS Best Paper Awards as well as the DLR Science Award.